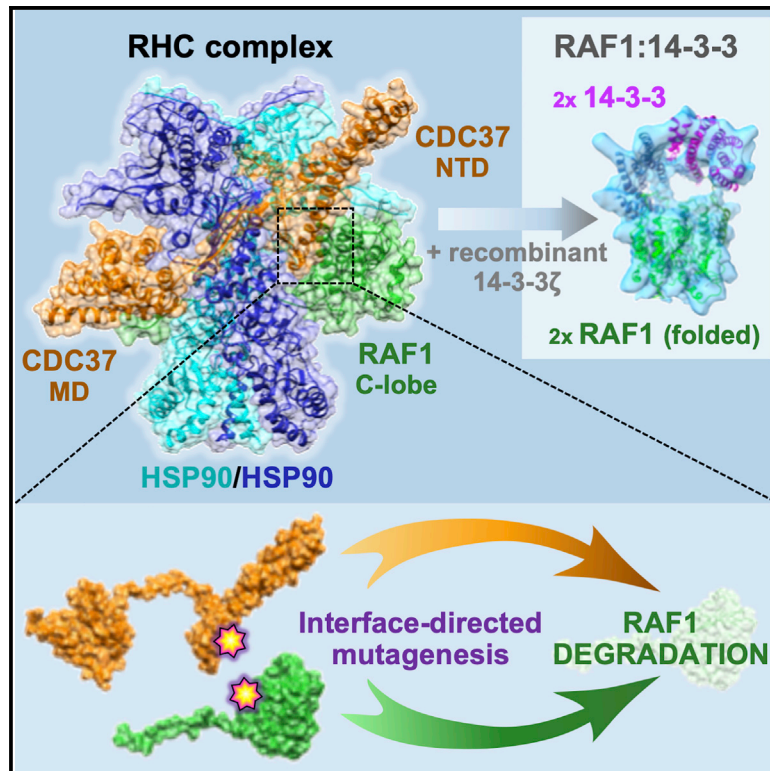


Structure of the RAF1-HSP90-CDC37 complex reveals the basis of RAF1 regulation

Graphical abstract



Authors

Sara García-Alonso, Pablo Mesa, Laura de la Puente Ovejero, ..., Jorge Martínez-Torrecuadrada, Mariano Barbacid, Guillermo Montoya

Correspondence

mbarbacid@cni.es (M.B.), guillermo.montoya@cpr.ku.dk (G.M.)

In brief

García-Alonso, Mesa et al. report the cryo-EM structure of the RAF1-HSP90-CDC37 (RHC) complex and how the folding of RAF1 regulates signaling. These data, combined with biochemical and functional assays, show that disruption of the complex reduces RAF1 protein levels and RAF1-dependent cellular proliferation, unveiling a therapeutic strategy in Kras/tp53-driven tumors.

Highlights

- Full-length RAF1 protein forms a stable complex with HSP90 and CDC37
- CDC37 can discriminate between the different members of the RAF family
- Folded RAF1 assembles with 14-3-3 dimers
- Disruption of the interaction between CDC37 and RAF1 causes the degradation of RAF1



Article

Structure of the RAF1-HSP90-CDC37 complex reveals the basis of RAF1 regulation

Sara García-Alonso,^{1,7,8} Pablo Mesa,^{2,8} Laura de la Puente Ovejero,¹ Gonzalo Aizpurua,¹ Carmen G. Lechuga,¹ Eduardo Zarzuela,³ Clara M. Santiveri,⁵ Manuel Sanclemente,¹ Javier Muñoz,³ Mónica Musteanu,⁶ Ramón Campos-Olivas,⁵ Jorge Martínez-Torrecuadrada,⁴ Mariano Barbacid,^{1,7,*} and Guillermo Montoya^{2,9,*}

¹Experimental Oncology Group, Molecular Oncology Programme, Centro Nacional de Investigaciones Oncológicas (CNIO), Madrid 28029, Spain

²Structural Molecular Biology Group, Novo Nordisk Foundation Centre for Protein Research, Faculty of Health and Medical Sciences, University of Copenhagen, Copenhagen 2200, Denmark

³Proteomics Unit, Biotechnology Programme, Centro Nacional de Investigaciones Oncológicas (CNIO), Madrid 28029, Spain

⁴Crystallography and Protein Engineering Unit, Structural Biology Programme, Centro Nacional de Investigaciones Oncológicas (CNIO), Madrid 28029, Spain

⁵Spectroscopy and NMR Unit, Structural Biology Programme, Centro Nacional de Investigaciones Oncológicas (CNIO), Madrid 28029, Spain

⁶Department Section of Biochemistry and Molecular Biology, Complutense University of Madrid, Madrid 28040, Spain

⁷Centro de Investigación Biomédica en Red de Cáncer (CIBERONC), Instituto de Salud Carlos III, 28029 Madrid, Spain

⁸These authors contributed equally

⁹Lead contact

*Correspondence: mbarbacid@cnio.es (M.B.), guillermo.montoya@cpr.ku.dk (G.M.)

<https://doi.org/10.1016/j.molcel.2022.08.012>

SUMMARY

RAF kinases are RAS-activated enzymes that initiate signaling through the MAPK cascade to control cellular proliferation, differentiation, and survival. Here, we describe the structure of the full-length RAF1 protein in complex with HSP90 and CDC37 obtained by cryoelectron microscopy. The reconstruction reveals a RAF1 kinase with an unfolded N-lobe separated from its C-lobe. The hydrophobic core of the N-lobe is trapped in the HSP90 dimer, while CDC37 wraps around the chaperone and interacts with the N- and C-lobes of the kinase. The structure indicates how CDC37 can discriminate between the different members of the RAF family. Our structural analysis also reveals that the folded RAF1 assembles with 14-3-3 dimers, suggesting that after folding RAF1 follows a similar activation as B-RAF. Finally, disruption of the interaction between CDC37 and the DFG segment of RAF1 unveils potential vulnerabilities in attempting the pharmacological degradation of RAF1 for therapeutic purposes.

INTRODUCTION

The RAF family of kinases (A-RAF, B-RAF, and RAF1, also known as C-RAF) are the direct KRAS effectors responsible for the activation of the mitogen-activated protein kinase (MAPK) signaling pathway (Matallanas et al., 2011). The three RAF proteins share a common modular structure consisting of three conserved regions (CRs) (Figure 1A). CR1 encompasses a RAS-binding domain (RBD), necessary for membrane recruitment, and a cysteine-rich domain (CRD), CR2 contains important inhibitory phosphorylation sites participating in RAF activation, and CR3 contains the kinase domain (Figure S1), whose phosphorylation is crucial for activation (Matallanas et al., 2011). The physiological regulation of RAF kinases is intricate and involves several steps including dimerization, protein-protein interactions, phosphorylation and dephosphorylation events, and conformational changes (Roskoski, 2010). In the absence of activating interactions with RAS, RAF proteins are thought to exist in a closed

autoinhibited conformation, stabilized by a dimer of the 14-3-3 phospho-binding protein, which is simultaneously associated to a phosphorylated N- and C-terminal sites of the kinase. Interaction of RAF kinases with membrane-bound RAS proteins with green fluorescent protein (GTP) leads to the activation of their kinase activity by a multistage process that requires phosphorylation at multiple sites within the N-terminal half of the protein, as well as dimerization of their kinase domains. The RAF kinases have restricted substrate specificity and catalyze the phosphorylation and activation of MEK1 and MEK2, their downstream effectors within the MAPK pathway (Roskoski, 2010). RAF1 is found in both the cytosolic and membrane fraction of cells as a component of a large multi-subunit protein complex including the chaperone HSP90 and the cochaperone CDC37 (Mitra et al., 2016; Morrison and Cutler, 1997; Wartmann and Davis, 1994).

HSP90 is a key regulator of proteostasis which associates with a number of co-chaperones that regulate the ATPase-associated



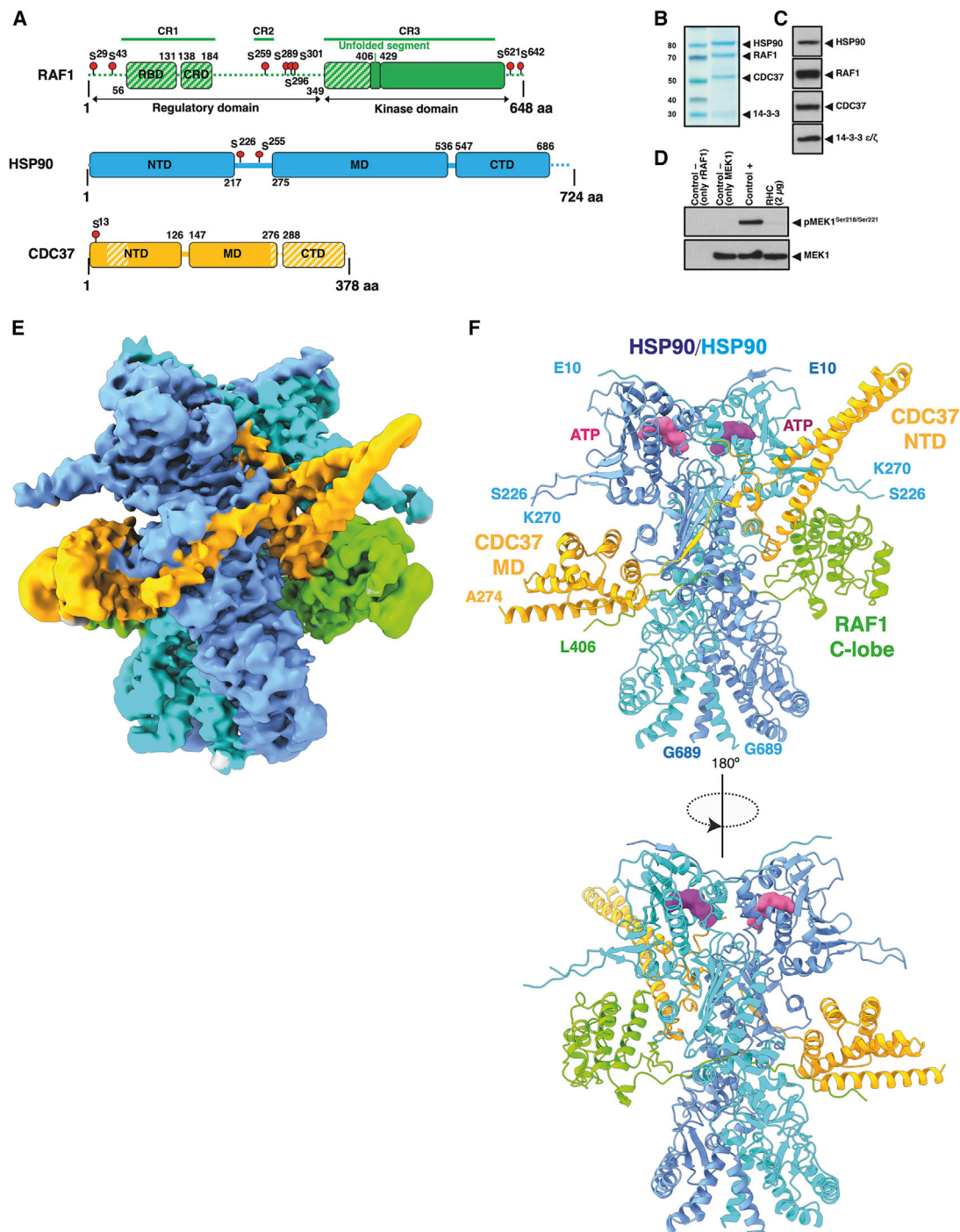


Figure 1. Biochemical characterization and cryo-EM structure of the RAF1-HSP90-CDC37 (RHC) complex

(A) Schematic diagram showing the domain organization of the proteins present in the RHC complex. The stripped/dashed parts indicate regions where there is no interpretable density. Red circles indicate phosphorylated residues identified by mass spectrometry (see also Table S1).

(B) Coomassie-stained SDS-PAGE showing the affinity purified complex from Expi293F mammalian cells. Endogenous 14-3-3 proteins copurified with the complex (see also Figure S2).

(C) Western blot analysis to confirm the protein composition of the isolated fractions. Migration of the corresponding proteins is indicated by solid arrowheads.

(D) *In vitro* protein kinase assay using recombinant MEK1 protein as a substrate.

(E) RHC-II cryo-EM map of the RAF1-HSP90-CDC37 complex at 3.67 Å global resolution. The map is colored according to each subunit as in Figure 1A (see also Figures S3 and S4; Table S2; Video S1), including blue and cyan for each monomer of the HSP90 dimer.

(F) Overview of the RAF1-HSP90-CDC37 assembly in complex with ATP (surface representation colored in pink and magenta).

conformational changes of the HSP90 dimer during the processing of clients (Schopf et al., 2017). The formation of the RAF1-HSP90-CDC37 (RHC) complex is crucial for RAF1 activity and MAPK pathway signaling (Grammatikakis et al., 1999), as the HSP90-CDC37 system facilitates RAF1 S621 phosphorylation and prevents protein degradation (Mitra et al., 2016). More than half of the human kinases are clients of the HSP90 molecular chaperone and its CDC37 cochaperone, which stabilize and activate them (Taipale et al., 2012). The structure at 4.0 Å of the CDK4-HSP90-CDC37 complex provided a first glimpse of the interaction of this chaperone system with a client kinase (Verba et al., 2016). However, these data do not provide the basis to understand why RAF1 and A-RAF, but not B-RAF, are part of its clients and how this interaction affects RAF1 regulation.

Based on their key role in MAPK signaling, RAF kinases have been long considered potential targets to block KRAS-mutant tumors. On the other hand, recent observations using genetically engineered mouse tumor models of *Kras/Trp53*-driven lung adenocarcinoma have demonstrated that ablation of RAF1, but not of B-RAF or A-RAF, results in significant levels of tumor regression without inducing unacceptable toxicities (Sanclémente et al., 2018). Moreover, expression of kinase dead isoforms of RAF1 does not result in therapeutic benefit, indicating that the contribution of RAF1 to the progression of KRAS-mutant lung adenocarcinomas is not mediated by its kinase activity (Sanclémente et al., 2021), thereby suggesting that RAF1 contributes to tumor progression by other mechanisms, mainly inactivation of apoptotic pathways (Mikula et al., 2001; Sanclémente et al., 2021). For yet unknown reasons, RAF1 ablation does not induce tumor regression in mice harboring pancreatic tumors induced by the same *Kras/Trp53* mutations. Yet, combined ablation of RAF1 and EGFR results in the complete regression of a subset of these tumors. These results strongly suggest that therapeutic strategies based on inhibition of RAF1 kinase activity are unlikely to produce anti-tumor results (Blasco et al., 2019). Hence, novel therapeutic approaches that result in the pharmacological degradation of RAF1 should be considered.

Here, we provide evidence illustrating why the HSP90-CDC37 system can discriminate between its clients RAF1 and A-RAF but does not chaperone wild-type B-RAF. CDC37 recognizes specific regions in the C-lobe of RAF1 and mutations in the main interacting regions of CDC37 and RAF1 dissociate the RAF1-HSP90-CDC37 complex. Furthermore, cell lines including these mutations display a reduced RAF1 content and cell progression. Both can be restored after expression of the wild-type RAF1, thus suggesting that disruption of the RHC complex represents a vulnerability that could render a therapeutic target for *Kras/Trp53*-driven tumors.

RESULTS

Isolation of the RHC complex

The RHC complex was isolated after transient co-expression in eukaryotic Expi293F cells (Figures 1B, 1C, and S2; STAR Methods). This complex consists of four polypeptides including HSP90, CDC37, and RAF1. Peptides for the α and β isoforms of

HSP90 were identified by mass spectrometry, and as determined by western blot analysis and mass spectrometry, a sub-stoichiometric amount of 14-3-3 phospho-binding proteins mainly, but not exclusively, composed of the ϵ/ζ isoforms, copurified with the RHC complex (Figure S2D). The mixture of α and β isoforms suggest that the endogenous HSP90 is also present in our sample, as we isolate the complex using a strep-tag in RAF1 (STAR Methods).

The isolated assembly shows phosphorylations in RAF1 key residues as well as in HSP90 and CDC37 (Figure 1A; Table S1). Yet, we could not observe any density for the 14-3-3 ϵ/ζ proteins in our cryoelectron microscopy (cryo-EM) analysis, even though the key S259 and S621 residues of RAF1 are phosphorylated (Figures 1E, 1F, S2F, S3, and S4), suggesting that these dimeric phospho-binding proteins do not associate with RAF1 when it is coupled with the HSP90-CDC37 chaperone system. In addition, we did not detect free molecules of RAF1 independent of the RHC complex, and the RHC did not significantly phosphorylate MEK1 (Figure 1D), indicating that RAF1 in complex with the HSP90-CDC37 system is inactive.

Overall structure of the RHC complex

We aimed to obtain structural information of the RHC complex by cryo-EM to understand how the HSP90-CDC37 system recognizes RAF1. The purified complex was isolated in the presence of molybdate to stabilize the substrate for cryo-EM (Hartson et al., 1999). The initial analysis of the RHC showed strong preferential orientation, and additional tilted images were collected to alleviate the associated anisotropy in the obtained maps (STAR Methods). This sample yielded a high-resolution map in which the RHC complex could be built but still suffered of preferential orientation (Figure S2F; STAR Methods). This effect was reduced after adding recombinant 14-3-3 ζ to the sample. However, 14-3-3 could not be observed associated to the RHC, but resulted in better reconstructions of the RHC complex, revealing the assembly of a fraction of RAF1 and 14-3-3. These new classes, not observed in the RHC sample without recombinant 14-3-3, allowed the reconstruction of a 7 Å map (Figure S3C; STAR Methods).

Using a combination of statistical classification and movie processing, we obtained the initial map at 3.59 Å global resolution of the RHC complex (RHC-0) (Figure S3C; STAR Methods). This map was highly heterogeneous, and thereby a second round of 3D classification was performed leading to a 3.16 Å resolution map (RHC-I), which displayed good density for the HSP90 dimer and the NTD of CDC37 but with high heterogeneity for the rest of the RHC regions. An alternative 3D classification was performed to improve the density in these heterogeneous regions, producing a map (RHC-II) at 3.67 Å global resolution (Figures 1E and S3C). This map allowed model building of the kinase C-lobe and CDC37 MD (Figure 1F; STAR Methods).

To understand the heterogeneity of the RHC complex, we performed an analysis of the variability of the RHC-0 map using cryoSPARC (Punjani et al., 2017) and cryoDRGN (Zhong et al., 2021), showing a large degree of flexibility localized at the RAF1 C-lobe and the visible regions of CDC37 MD. In addition, we observed that the two lateral moieties of the RHC complex behave independently, thus illustrating its large plasticity

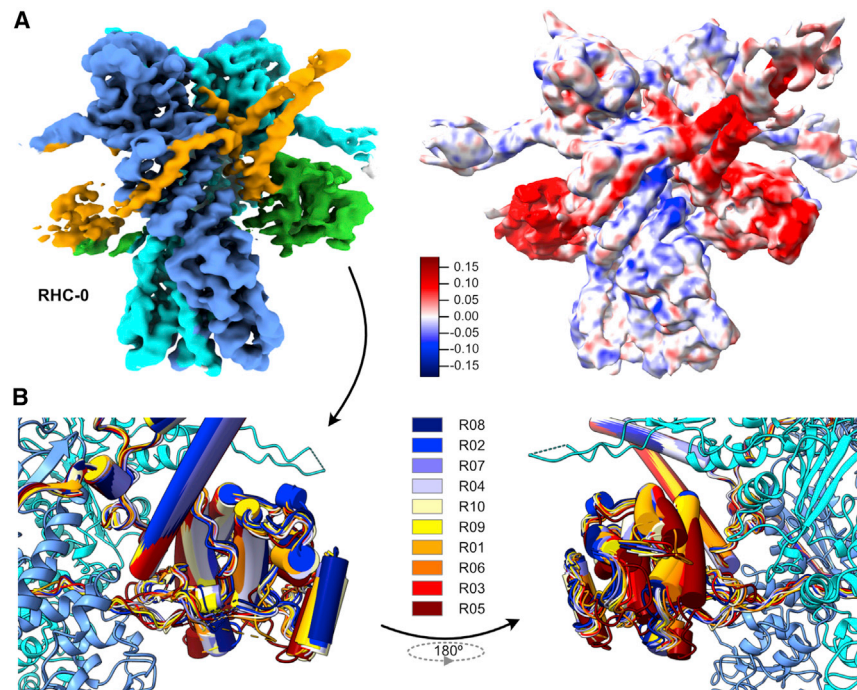


Figure 2. Conformational heterogeneity of the RHC complex associated with the movement of RAF1 C-lobe

(A) 3D variability analysis (right panel, cryoSPARC) of a subset of 442-k particles of the RHC complex (left panel; see Figure S3C). The 3D reconstruction obtained from those particles is colored according to one dimension of the variability (from blue to red; see also Video S1) (Punjani and Fleet, 2021).

(B) A localized 3D classification of these particles produced a series of maps (R01-10, Figure S5B) and RAF1 C-lobe models were fitted and refined into them, showing that the heterogeneity in that region can be described as the free rotation of the C-lobe around a fulcrum defined by its interaction with CDC37, and the entry point into HSP90 of the extended segment of RAF1 N-lobe (see also Videos S1 and S2).

(Figures 2 and S5; STAR Methods). A local focused classification in the C-lobe of RAF1 resolved the continuous flexibility of the sample representing different conformations of the assembly (Figures 2B and S5B; Video S1).

The core of the RHC complex, specially HSP90, was visualized at high resolution without applying 2-fold symmetry; while the CR1 and CR2 regions of RAF1, as well as part of the N-terminal lobe of the kinase domain and the N- and C-terminal domains (NTD and CTD) of CDC37 were not visible in these density maps (Figures 1A, 1E, 1F, and 2), indicating the large mobility of these regions. In addition, changes in the conformation of the identified domains could be also observed between the different maps (Figure S5; Videos S1 and S2). Both maps were of sufficient quality to accurately build and refine atomic models of the RAF1-HSP90-CDC37 complex (Table S2; Figure S4).

HSP90 separates the N- and C-lobes of RAF1

The HSP90 dimer adopts a conformation that closely resembles its closed state, as previously observed in the CDK4-HSP90-CDC37 structure (Verba et al., 2016). A segment of RAF1 is associated with the mapped HSP90 client binding site. Inside the lumen formed by the HSP90 MD, we observed an elongated polypeptide comprising part of the N-lobe and the connection with the C-lobe of the RAF1 kinase domain (Figures 3A and 3B). This segment (L406 to W429) encompasses the complete β 4 and β 5 sheets, the connecting loops, and the first turn of the α C helix of the RAF1 kinase domain. This unfolded region constitutes the core of the RAF1 kinase N-lobe associated with HSP90. Except the initial turn of the α D helix, the rest of the C-lobe of RAF1 is folded and can be superimposed with the corresponding region of the RAF1 crystal structure with only 1.2 Å RMSD (151 $C\alpha$ atoms, PDB:3OMV) (Figure S6A). Collectively,

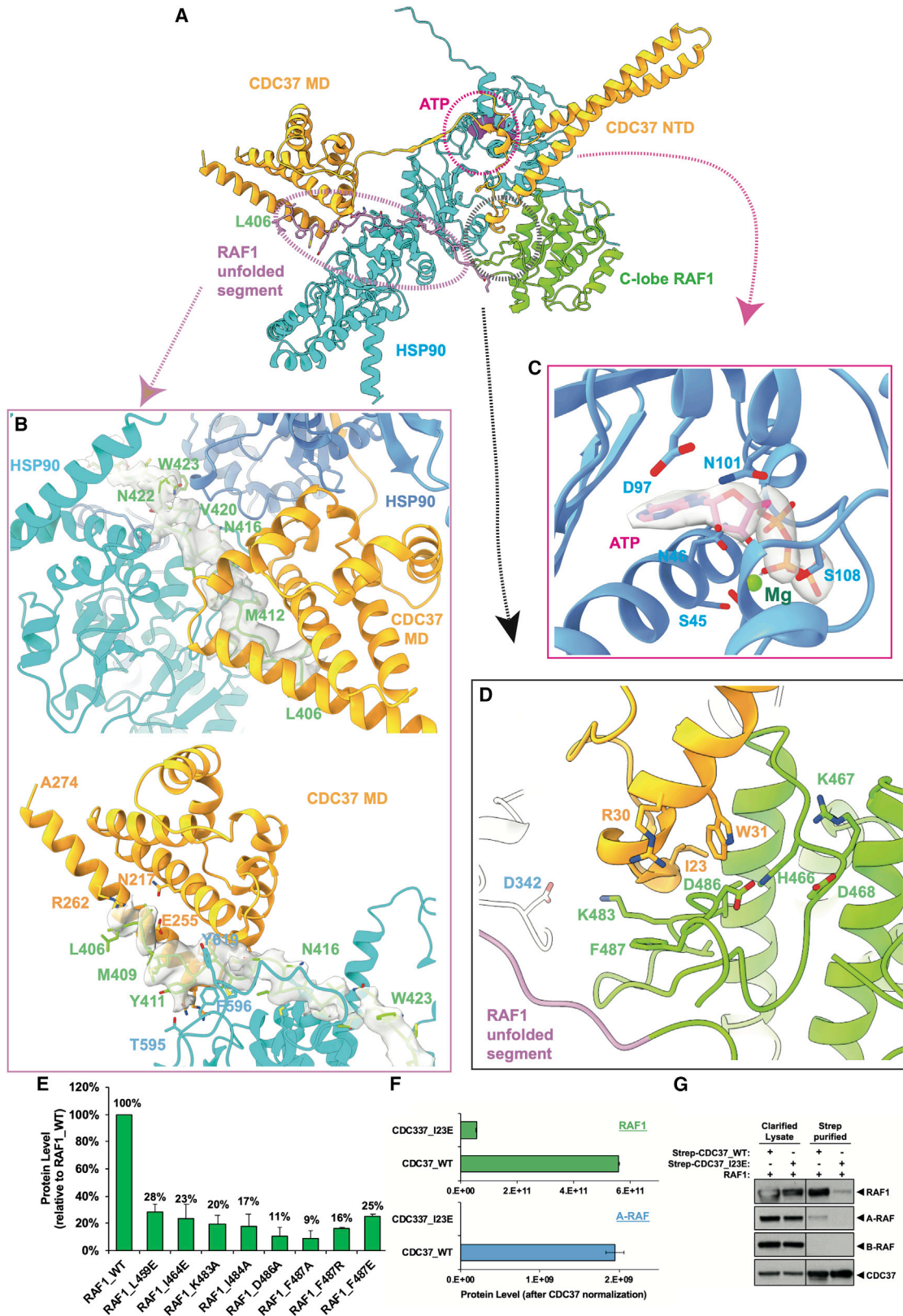
the data suggest that the N-lobe of RAF1 is unfolded in our structure because the association of the central β strands composing the N-lobe with the chaperone would disturb the folding of this subdomain when RAF1 is associated to HSP90-CDC37.

The RAF1 residues ranging from W429 to L417 interact with the binding pocket of the HSP90 via extensive hydrophobic interactions (Genest et al., 2013). Only a polar interaction between R612, in one of the HSP90 chains, and RAF1 E425 at the entrance of the HSP90 cleft, can be observed (Figures 3A, 3B, and S6B). The HSP90 protomers collaborate in stabilizing the elongated hydrophobic segment; however, one of the HSP90 monomers (HSP90 cyan monomer in Figure 3, corresponding to chain B in our structure) displays a larger number of hydrophobic contacts, revealing an asymmetric interaction of the unfolded kinase lobe with the chaperone. This asymmetric association of the substrate is related to the proposed mechanism used by the MD-CTD interface of HSP90 to link its nucleotide hydrolysis state to the associated client (Lavery et al., 2014).

The HSP90 nucleotide-binding pockets are occupied. Although molybdate is proposed to act as a post hydrolysis transition state inhibitor, thus helping to stabilize the HSP90 closed conformation, its mode of action is unclear (Hartson et al., 1999). Our results suggest that molybdate stabilization does not seem related to the nucleotide hydrolysis. The highest density value in the maps of the RHC complex is observed in the β - and γ -phosphates of the ATP molecule, suggesting that the complex traps HSP90 in an ATP bound state, as the bond between both phosphates appears to be intact (Figures 3C, S3, and S4). However, we cannot fully disregard that ADP-molybdate could act as an inhibitor, locking off the post-hydrolysis transition state.

CDC37 interacts with the N- and C-lobes of RAF1

The CDC37 NTD and middle domain (MTD)/CTD are also separated by the HSP90 dimer. The helical N-terminal contains a leucine zipper like motif and is adjacent to the C-lobe of the kinase in the same face of HSP90. This region is linked with the



(legend on next page)

CTD by a β strand which flanks the HSP90 MD of one monomer, building an antiparallel β sheet with the MD of this monomer. The β strand is connected to the C-terminal density on the other side of the HSP90 dimer where CDC37 makes contacts with the residues 406–415 of RAF1 (Figures 3A, 3B, and S6C). We were able to unambiguously resolve the structure until residue S300 of CDC37, thus visualizing the interaction of this region with the visible part of the N-lobe of RAF1 (Figures 3A–3C).

The C-lobe of RAF1 is stabilized by a combination of polar and hydrophobic contacts with the helical region of the NTD of CDC37. The residues T19 to R32 in CDC37 engage in interactions with the activation loop of RAF1, including the conserved DFG and HRD kinase family motifs, and the residues Q451 to I465 in the region of the α C and α D helices of RAF1 (Figures 3D, S6D, and S6E). The loop between residues T19 to T25 in CDC37 superimposes with the loop between α C and β 4 of the RAF1 kinase domain structure, suggesting that the CDC37 NTD associates with the C-lobe by mimicking the interactions with a folded RAF1 N-lobe, thus stabilizing the separated C-lobe moiety. Our analysis permits the identification of these stabilizing interactions of HSP90-CDC37 with the elongated RAF1 kinase domain, and it shows the flexibility of this association (Figures 2 and S5; Videos S1 and S2).

The phosphorylation of S13 in CDC37 is important to promote kinase function (Vaughan et al., 2008). We visualize the phosphate group in S13, which makes polar interactions with R36 and H33 in CDC37 and K406 in the corresponding monomer of HSP90 (Figure S6F). The phosphorylation stabilizes the N terminus of the helical NTD of CDC37 and thereby favors the association of the antiparallel β strand with HSP90. The arrangement promoted by S13 phosphorylation in the RHC complex is similar to that observed in the CDK4/HSP90/CDC37 complex (Verba et al., 2016), suggesting that this phosphorylation is a conserved mechanism of the HSP90-CDC37 system to promote the conformation leading to the interaction with the client independently of the kinase sequence (Verba et al., 2016).

After the unfolded segment that interacts with the HSP90 lumen, the D415 to I406 section of the unfolded RAF1 N-lobe associates with the MD/CTD of CDC37 and engages in hydrophobic and polar interactions with residues M606, M620, Y596, Y619, and T595 with the HSP90 in one monomer. The D245, R246, and Q247 residues in CDC37 are also involved in that interaction. The rest of the visualized unfolded N-lobe, ranging from Y411 to I406, lies on a cavity made by two helices where

it engages in polar contacts with R262, E255, N217, and K257 residues in CDC37 (Figures 3A and 3B). The high mobility in this area hindered the observation of the rest of the N-lobe and the CTD of CDC37 (Figures 2 and S5).

RAF1 and CDK4 association to the HSP90-CDC37 system

Overall, the structures of RAF1 and CDK4 bound to HSP90-CDC37 are similar (Figure 4A). The phosphorylation of the helical NTD of CDC37 is conserved in both structures and seems to be an important common feature for HSP90-CDC37 kinase clients (Figure S6F). In addition, the loop in the NTD of CDC37, which stabilizes the C-lobes of the open kinase domains, displays a similar conformation (Figures S6D and S6E). However, the regions of CDK4 and RAF1 C-lobes interacting with the loop show different conformations, suggesting that the stabilization of the C-lobe in the open kinase client follows a similar approach, but it can display local differences depending on the specific kinase (Figure 4B).

The structural comparison reveals that the region of the N-lobe interacting with HSP90 lies in the β sheet region in a folded kinase domain but includes different elements of the secondary structure in both kinases. In the case of CDK4, only β 4 and the loop joining the N- and C-lobes of CDK4 is observed associated to HSP90-CDC37. However, for RAF1, in addition to that region, the β 5 strand and a section of the following loop is associated to HSP90 and the MD of CDC37 (Figures 4C, 4D, S1, and S6A–S6D). Therefore, in both kinases, the folding of the N-lobe should be disturbed, as the antiparallel β sheet building that subdomain could not assemble (Figure 4C). This seems to be the case for RAF1 (Figures 2 and S5), where we cannot assign any clear density to the N-lobe; instead, we observe residues of that region interacting with the MD of CDC37 (Figures S6B and S6C). However, in the case of CDK4, while the N-lobe is significantly unfolded (Verba et al., 2016), 3D classification has shown distinct low-resolution globular densities, allowing docking of the remainder of its N-lobe. This difference could suggest that the degree of unfolding of the N-lobe for different kinase clients when associated to HSP90-CDC37 is different and would depend on the secondary structure and the extension of the region interacting with HSP90-CDC37. These differences could affect the kinase-folding efficiency of the HSP90-CDC37 system, suggesting another possible regulatory aspect involving not only the folding of an active enzyme but also the efficiency of the folding process, as client kinases that conserve some regions of the N-lobe

Figure 3. Interactions of RAF1 with HSP90 and CDC37 in the RHC complex

(A) Overall view of the RHC complex. A monomer of HSP90 is omitted to show the region of RAF1 passing through the chaperone lumen and its interaction with CDC37.

(B) The top panel shows a view of the cryo-EM map of the L406–L429 region of RAF1. The bottom panel depicts a view of the L406–L417 region of RAF1 that interacts with the MD/CTD domain of CDC37 (see also Figure S6).

(C) View of the cryo-EM map around one of the ATP molecules at the NTD of HSP90.

(D) Detailed view of the main interacting region between CDC37 and RAF1 in the RHC complex.

(E) Levels of wild-type and mutant RAF1 proteins co-expressed with HSP90 and CDC37 in Expi293F cells after strep-tag isolation from clarified cell lysates. The levels of each protein were quantified by mass spectrometry, using RAF1 common peptides for all the mutants. The graph shows the mean protein level, normalized to RAF1 wild type, of three different experiments. Error bars indicate standard deviation.

(F) Mean levels of RAF1 and A-RAF bound to strep-tagged wild-type CDC37 and mutant CDC37 I23E proteins. B-RAF peptides were undetectable (not shown). Error bars indicate standard deviation.

(G) Western blotting analysis of clarified cell lysates and pull-downs from the experiment described in (F). Note that the endogenous A-RAF protein co-purified with wild type but not with mutant CDC37. Migration of the corresponding proteins is indicated by solid arrowheads.

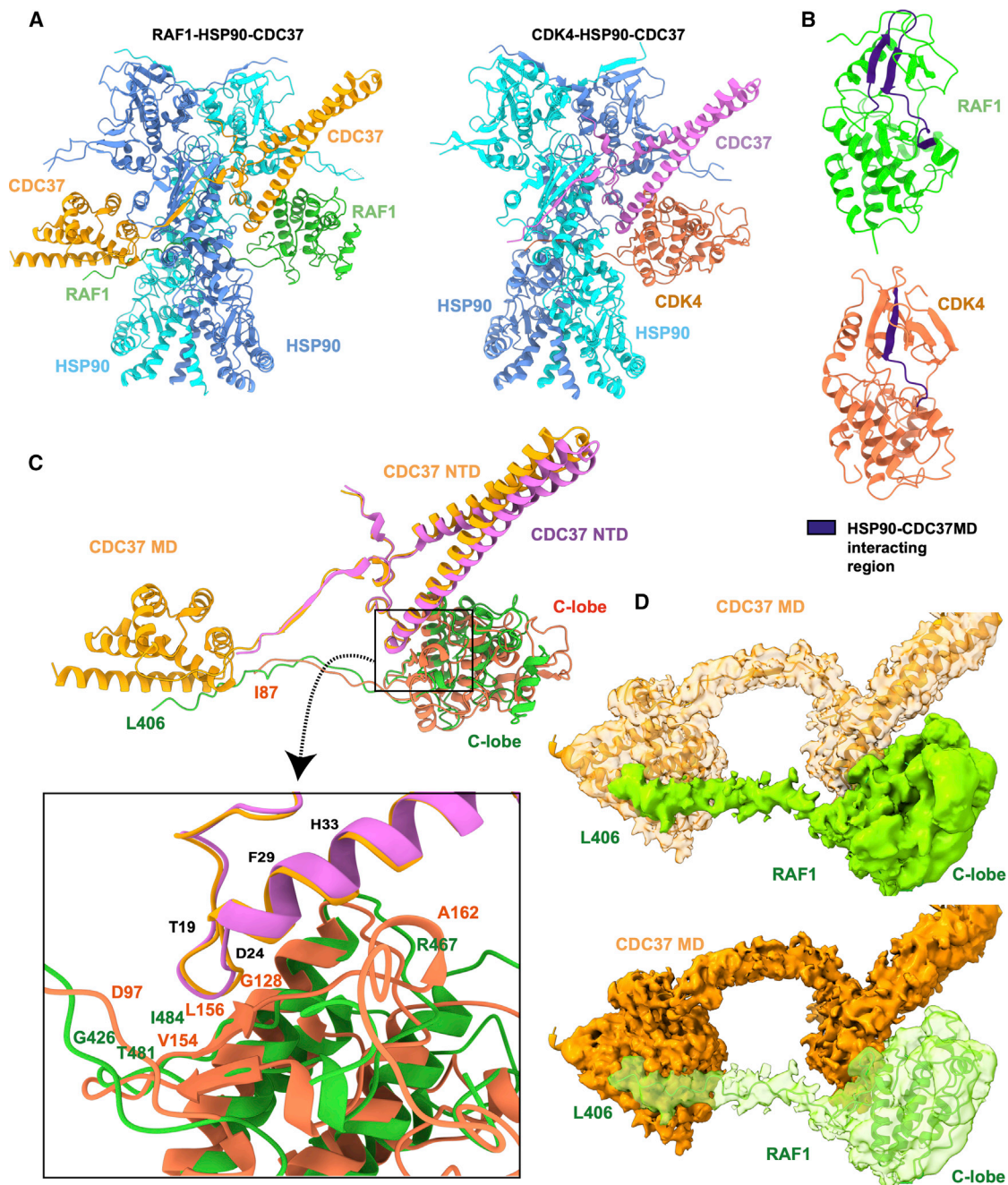


Figure 4. Comparison of the RAF1 and CDK4 structures in complex with the HSP90-CDC37 system

(A) Ribbon diagram of the RHC and CDK4-HSP90-CDC37 (PDB:5FWK) complexes.

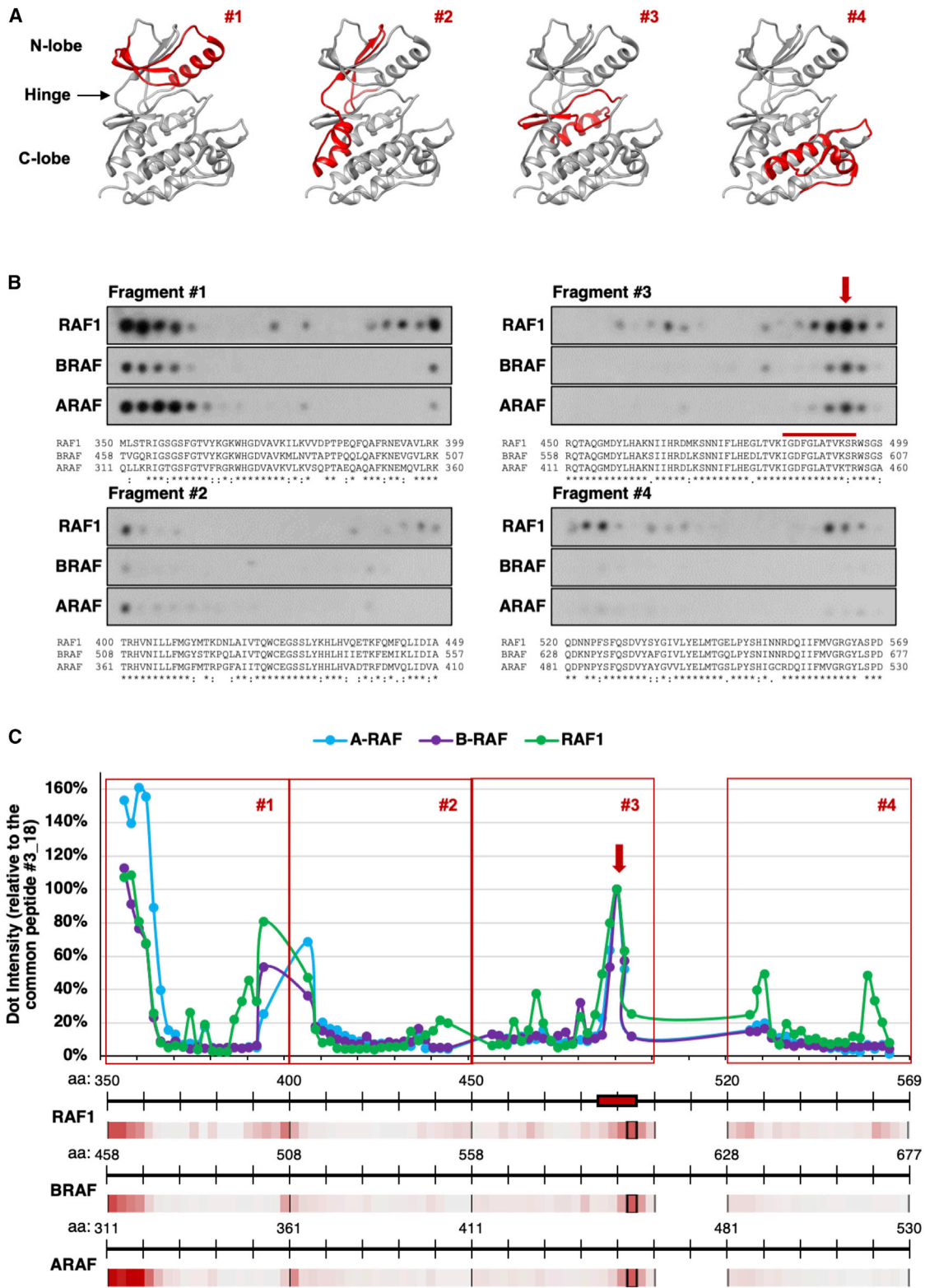
(B) Superposition of the crystal structures of RAF1 (PDB:3OMV) and CDK4 (PDB:2W9Z) showing the different elements of secondary structure involved in the interaction with HSP90 and CDC37 MD. (C) View of the CDC37 kinase client interaction. The HSP90 dimer has been omitted for clarity. The inset depicts the differences in the interaction of the CDC37 NTD loop (residues 19–32) with the C-lobe of RAF1 and CDK4.

(D) View of the cryo-EM density map showing the interaction of CDC37 with RAF1.

folded would be easier to become functional, while those with an unfolded N-lobe would be less efficiently folded, thereby influencing their activity. Further studies will be needed to test whether HSP90 folding efficiency of different kinase clients is different, thus influencing their cellular activity.

Recombinant 14-3-3 ζ phosphobinding protein promotes the dissociation of the RHC complex

As indicated above, RAF1 is phosphorylated in S259 and S621 in the RHC complex (Figure 1A; Table S1). These residues are equivalent to S365 and S729 in B-RAF, that are associated to



(legend on next page)

14-3-3 proteins in different B-RAF complexes (Kondo et al., 2019; Park et al., 2019). Although 14-3-3 ϵ/ζ proteins copurified with the RHC complex, we could not detect stable complexes of RAF1 with these phosphate-binding proteins (Figures S2F and S3C). Thus, we incubated recombinant 14-3-3 ζ with the isolated RHC complex and analyzed the sample by cryo-EM. While a substantial fraction of the observed particles still belongs to the RHC complex without 14-3-3, a new type of particles appeared in the sample and could be separated *in silico*. The reconstruction of the new particles at 7 Å allowed us to model a dimer of the RAF1 kinase associated to a 14-3-3 dimer using their crystal structures (Figures S3 and S7). This structure is similar to those of B-RAF/14-3-3 complexes (Kondo et al., 2019; Fiesco et al., 2022), which have provided an explanation for the mechanism of the activation of B-RAF. Therefore, our observations suggest that the high concentration of 14-3-3 in the sample promotes binding of the phosphorylated-folded RAF1 protein upon its release from the RHC complex. Whether RAF1 is folded by the chaperones prior to its release or after binding to 14-3-3 remains to be determined. However, the fact that RAF1 is stabilized by the HSP90-CDC37 strongly indicates that association to the phosphate-binding proteins occurs when the kinase domain is folded. Therefore, our data suggest that RAF1 activation may follow a similar mechanism to that of B-RAF, after its folding by the HSP90-CDC37 system. Unfortunately, the low resolution of the map does not allow us to visualize if the RAF1 dimer is arranged in the same fashion as B-RAF (Kondo et al., 2019).

Disruption of the interaction between CDC37 and RAF1 affects protein stability

To investigate the functional relevance of the interactions observed within the structure of the RHC complex, we isolated complexes formed between eight different RAF1 mutants co-expressed with HSP90 and CDC37 in Expi293F cells. The relative levels of the mutant RAF1 proteins in the isolated RHC complexes were assessed by mass spectrometry and compared to those formed by the wild-type protein. Mutation of key residues in the interface between RAF1 and CDC37 reduced the level of RAF1 protein present in the complexes between 70% and 90% (Figure 3E). Likewise, expression of a CDC37 protein carrying the I23E mutation, a residue located in the loop that stabilizes the C-lobe of RAF1 (Figure 3D), with wild-type RAF1, strongly affected the amount of RAF1 present in the RHC complex. Similar results were observed for the endogenous A-RAF protein, highlighting the importance of this residue in the stabilization of the C-lobe (Figures 3F and 3G; STAR Methods). As ex-

pected, B-RAF did not copurify with CDC37 in any case. Collectively, the site-directed mutagenesis data support the importance of the interactions observed between CDC37 and the C-lobe of RAF1 and suggest that the client kinase is degraded when its association with the HSP90-CDC37 system is disturbed.

Structural basis for the HSP90-CDC37 discrimination between RAF proteins

The interactions observed within the RHC complex prompted us to investigate the molecular bases for the different association of the three RAF proteins with the HSP90-CDC37 system. A previous study concluded that the binding determinants of the RAF kinases to HSP90 are widely distributed in both lobes of their kinase domain and act in a combinatorial way to determine the interaction (Taipale et al., 2012). Our structure shows that HSP90 interacts with residues that, in the mature folded structure, would form the hydrophobic core of RAF1 N-lobe, as previously shown for the CDK4/HSP90/CDC37 complex (Verba et al., 2016), while CDC37 seems to recognize different regions of the RAF1 kinase domain and combines the non-polar contacts with polar interactions.

To test whether CDC37 can recognize specific segments of the various RAF kinases, we performed a binding assay incubating this cochaperone with a nitrocellulose-bound dodecapeptide array (PepScan) displaying the corresponding sequences of RAF1, B-RAF, and A-RAF kinase domains (Figure 5). The assay shows that CDC37 can bind and is able to discriminate between the different dodecapeptides in the absence of HSP90. Noteworthy, CDC37 does not bind the region of RAF1 interacting with HSP90. Instead, the array shows that, despite some sequence differences, CDC37 recognizes a region in the N-lobe common to the three RAF family members (residues M350-W368, RAF1 numbering) including the GSGSFG motif (Terasawa et al., 2006). In addition, CDC37 interacts preferentially with another segment of RAF1 (P384-T400), not conserved in the other RAF proteins. This segment includes the loop joining α C with β 4 (A395-T400) (Prince and Matts, 2004), which is found stabilizing the C-lobe of the unfolded RAF1 kinase domain (Figures 3A, 3D, S6D, and S6E), as previously observed in CDK4 (Verba et al., 2016). Residues V482 to G498 display another high intensity PepScan binding site common to the three members of the RAF family. Finally, the C-lobe of RAF1 shows two specific binding sites in the P524-I536 and M560-K572 segments, which display minor sequence differences (Figures 5B, 5C, and S1). Therefore, CDC37 binds to different regions within the members of the RAF family. While

Figure 5. Recognition of RAF sequences by CDC37

(A) Schematic diagrams showing the general structure of the kinase domain of RAF family members. The four fragments analyzed by PepScan, covering the whole kinase domain, are highlighted in red (see also Table S3).

(B) CDC37 binding assay on nitrocellulose-bound RAF peptides (PepScan). Overlapping dodecapeptides with a shift of two amino acids residues scanning the indicated regions of the kinase domains of human RAF1, B-RAF, and A-RAF proteins developed by enhanced chemiluminescence (ECL) after incubation with purified CDC37. The sequences covered by these dodecapeptides are indicated below each set of membranes.

(C) Quantification of the PepScan assay for the sequences of the (green) RAF1, (purple) B-RAF, and (blue) A-RAF kinase domains. The RAF1 peptide that interacts with CDC37 according to the cryo-EM structure is indicated with a red arrow. The CDC37 binding intensity to each peptide was calculated as the mean pixel integrated density of each dot relative to a reference one, with a common sequence among RAF family members (peptide 18 from region #3). The dot intensity is also shown as a color-scale (light gray to red), with the reference dot marked by a black square.

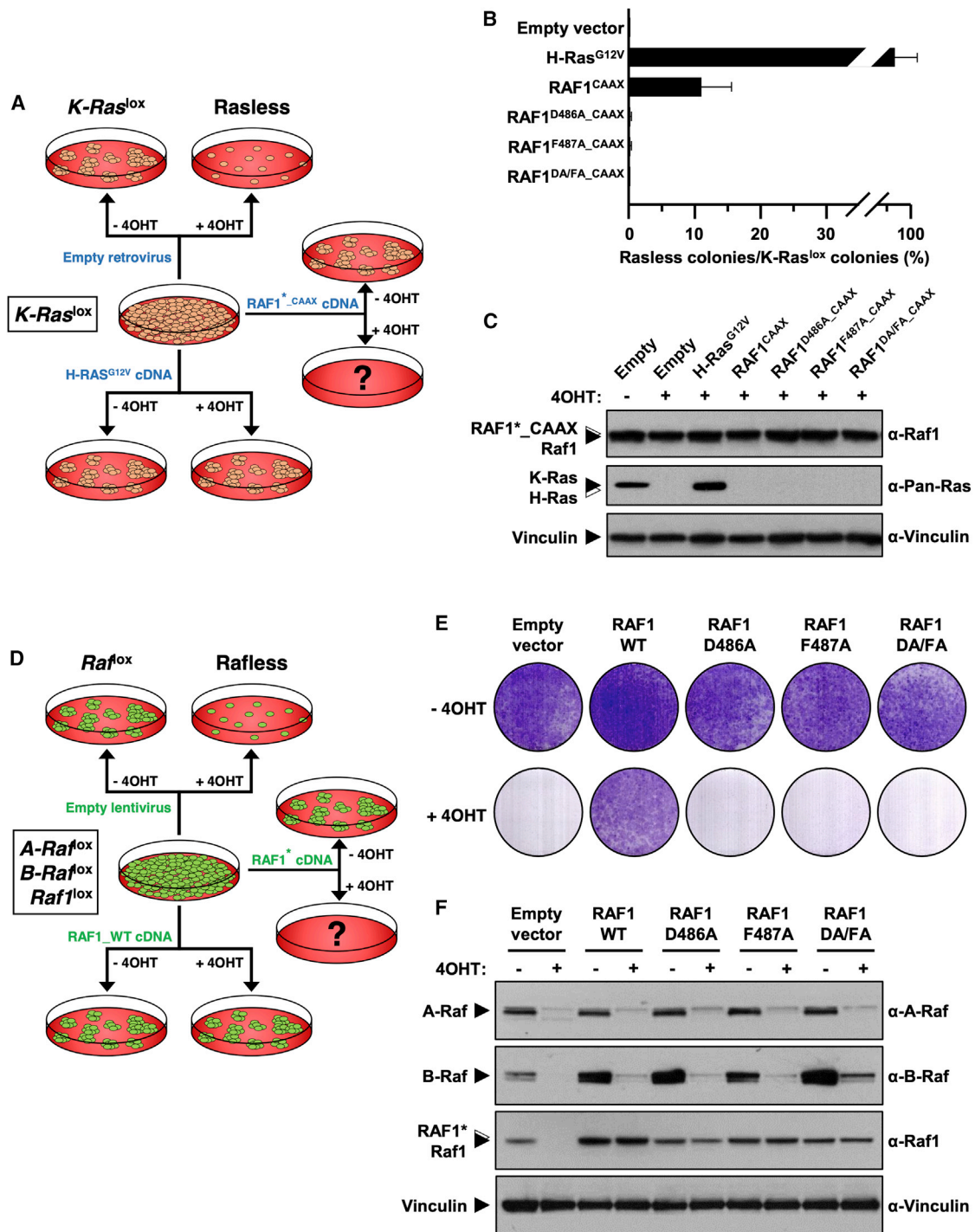


Figure 6. Disruption of the interaction between CDC37 and RAF1 inhibits cell proliferation

(A) Schematic representation of the *Rasless* colony assay used to evaluate the capacity of *RAF1* mutants to induce cell proliferation.

(B) Colony-formation assay using *K-Ras^{lox}* MEFs infected with retroviruses expressing the indicated cDNAs. Error bars indicate standard deviation.

(C) Western blot analysis showing levels of expression of the indicated H-Ras^{G12V} or *RAF1* CAAX proteins in *K-Ras^{lox}* MEFs. Cells were either (-) left untreated or (+) exposed to 4OHT, to eliminate *Kras* expression. Probing antibodies are indicated in the right panel. Migration of the corresponding proteins is indicated by solid arrowheads. Open arrowheads indicate migration of the exogenous proteins. Vinculin expression served as loading control.

(legend continued on next page)

several of these segments are shared among the three RAF proteins, the CDC37 cochaperone also associates with specific regions present in the RAF1 kinase domain, suggesting that the combination of the common and the exclusive sites is used by CDC37 to discriminate between the three family members.

Disruption of the RAF1-CDC37 interface decreases RAF1-dependent proliferation

As illustrated above, the assembly of the RHC complex is severely reduced in D486A and F487A RAF1 mutants (Figure 3E). To evaluate the effect of these single mutations as well as the D486A/F487A double substitution in cell proliferation, we took advantage of *H-Ras*^{-/-}, *N-Ras*^{-/-}, *K-Ras*^{lox/lox} (*K-Ras*^{lox}) mouse embryonic fibroblasts (MEFs), which are known to cease proliferation upon ablation of KRAS expression (*Rasless* cells) (Figure 6A). Ectopic expression of RAF1 in these cells restores cell proliferation through its interaction with the plasma membrane via addition of CAAX sequences derived from RAS proteins as long as p16INK4A expression is downregulated to avoid cell senescence (Drosten et al., 2010; Lechuga et al., 2021). We observed that the ectopic expression of wild-type RAF1, but not the D486A, F487A, and D486A/F487A mutants, elicited efficient proliferation of *Rasless* cells as determined in a colony-forming assay (Figures 6B and 6C). To validate this effect in cell proliferation, we use an additional cell model: *A-Raf*^{lox/lox}, *B-Raf*^{lox/lox}, *Raf1*^{lox/lox} (*Raf*^{lox}) MEFs, which also cease proliferation upon ablation of all RAF family members' expression (*Rafless* cells) (Figure 6D). Ectopic expression of wild-type RAF1 in these cells completely restored cell proliferation, albeit the absence of A-Raf and B-Raf. Contrarily, we observed that the ectopic expression of the mutant forms of RAF1 (D486A, F487A, and D486A/F487A) did not promote proliferation of *Rafless* cells as determined in a colony-forming assay (Figures 6E and 6F). Thus, disruption of the interaction between the RAF1 mutants and CDC37 hinders cell proliferation most likely due to the instability of the RAF1 mutants. However, due to the ectopic expression of the mutants, complete degradation of the protein is not achieved. Thus, we cannot rule out the possibility that the absence of kinase activity plays a role in preventing cell proliferation.

DISCUSSION

In this study, we visualize how RAF1 assembly with HSP90 and CDC37 is crucial for its stability and consequent activation (Grammatikakis et al., 1999) and prevents its degradation (Mitra et al., 2016), since the RHC complex maintains RAF1 in an inactive form. Thus, the open partially folded intermediate of RAF1 observed in the RHC complex plays a key regulatory role in controlling signaling through the MAP kinase cascade and cellular proliferation. Our data reveal that the structural principles of RAF1 kinase recognition by the HSP90-CDC37 system are

similar to those observed in its complex with CDK4 (Verba et al., 2016). The complex displays a high flexibility, which is most likely indispensable when its function is to keep RAF1 kinase domain in a stable but quasi folded state. The mimicking of the loop joining α C with β 4 (Prince and Matts, 2004) in the kinase domain by CDC37 is a conserved feature of the HSP90-CDC37 complex, which explains the importance of the phosphorylation in the S13 residue of CDC37, as the phosphate group builds the interactions that promote the conformation to stabilize the folded C-lobe of RAF1. We also observed that a section of the unfolded N-lobe which emerges from the HSP90 binding site is stabilized by the MD/CTD region of CDC37.

Despite their well-conserved sequence, members of the RAF family contain substantial functional differences. RAF1 and A-RAF are client proteins of the HSP90-CDC37 chaperone system, while B-RAF is not. Therefore, the HSP90-CDC37 chaperone system adds an extra regulatory layer to this kinase family. A key question in their intricate regulation is how the HSP90-CDC37 system can discriminate between them. Strong HSP90-CDC37 clients have been characterized to be less thermodynamically stable on their own, while more stable clients display reduced dependence for maturation (Taipale et al., 2012). The structure of the RHC highlights the key interactions of the HSP90 chaperone and its cochaperone CDC37 with RAF1. Moreover, our combined biochemical and functional analysis of the interacting regions indicates that CDC37 can recognize segments of RAF1 that are different from their counterparts in B-RAF. In addition, the comparison of the crystal structures of RAF1 and B-RAF kinase domains suggest that the 480–505 region of RAF1, which is important in the interaction with CDC37, displays different structural features. This region is disordered in RAF1, while it is structured in B-RAF (Figure S7C). Even though a direct comparison may be influenced by the different experimental conditions, the sequence differences seem to promote a different stability of this section of the kinase domain that interacts with CDC37. Our data suggest that discrimination between B-RAF and RAF1 by HSP90-CDC37 arises from the combined effect of the recognition of some specific sites of RAF1 by CDC37 and the different stability of the kinase domains, which could make the main binding site preferentially available for CDC37 binding in the case of RAF1. Likewise, this may be the case for A-RAF; however, its kinase domain structure is not available for comparison.

This conclusion is also supported by the fact that the B-RAF V600E oncogenic mutant is a client of the HSP90-CDC37 system (Diedrich et al., 2017; Grbovic et al., 2006), which is in agreement with the proposed destabilization of the kinase inactive state by the V600E mutation by disrupting hydrophobic interactions present in the wild type, while the active state would be stabilized through the formation of a salt bridge between E600 and K507 residues (Maloney et al., 2021). This notion is also supported by the fact that the crystal structures of the B-RAF V600E mutant

(D) Schematic representation of the *Rafless* colony assay used to evaluate the capacity of RAF1 mutants to induce cell proliferation.

(E) Colony-formation assay using *Raf*^{lox} MEFs infected with lentiviruses expressing the indicated cDNAs.

(F) Western blot analysis showing levels of expression of the indicated proteins in *Raf*^{lox} MEFs. Cells were either (–) left untreated or (+) exposed to 4OHT, to eliminate *A-Raf*, *B-Raf*, and *Raf1* expression. Probing antibodies are indicated in the right panel. Migration of the corresponding proteins is indicated by solid arrowheads. Open arrowheads indicate migration of the exogenous proteins. Vinculin expression served as loading control.

(PDB:4MNF, PDB:6P3D) display a disordered 480–505 region similar to that observed in RAF1 (Figure S7C). Therefore, in the case of B-RAF V600E, the HSP90-CDC37 system could assist the folding of the oncogenic mutant by promoting an active stable kinase which triggers malignant transformation. Collectively, our data suggest that recognition of the client kinase by CDC37 would depend on the binding sites of the target polypeptide and the availability of these regions to associate with CDC37, which is controlled by the global stability of the protein.

Our mutagenesis analysis of the interface between CDC37 and RAF1 highlights the importance of this association for RAF1 stability. Indeed, we observed a reduction in the levels of RAF1 when the mutant isoforms were co-expressed with HSP90 and CDC37. In addition, germline expression of a RAF1 D486A mutant in mice led to embryonic death during mid-gestation due to the absence of RAF1 expression, a result likely to be due to the instability of this mutant protein (Noble et al., 2008). As illustrated here, RAF1 mutations in this interface affect cell proliferation, since the mutant RAF1 proteins were not able to induce proliferation of MEF when ectopically attached to the plasma membrane in the absence of RAS proteins. Similar results were obtained in an additional cell model when all RAF family members were genetically ablated. These observations raise the possibility that the interface between RAF1 and CDC37 may represent a vulnerable spot, which could be targeted to induce the degradation of RAF1, reproducing the therapeutic results obtained in experimental models of *Kras/Trp53*-induced lung tumors upon ablation of RAF1 expression (Sanclemente et al., 2018).

We propose a model in which RAF1 would be unstable until it becomes associated with CDC37, and the cochaperone will associate with the kinase on the basis of its conformational stability (Keramisanou et al., 2016), followed by binding to HSP90, thereby leading to the formation of the RHC complex (Figure 7). The HSP90-CDC37 chaperone system couples the folding of the client protein with ATP hydrolysis cycles (Figure 7A). RAF1 is phosphorylated in residues S259 and S621, thereby, once the HSP90-CDC37 renders this protein folded, the RHC complex is disrupted and RAF1 associates with 14-3-3 (Figure 7A). One possibility by analogy with B-RAF is that RAF1 forms an autoinhibited state (Park et al., 2019), which could be released upon interaction with RAS; however, we have not observed it. Although the low resolution cryo-EM structure of RAF1 associated with 14-3-3 limits a detailed interpretation, our data shows that the RAF1 protein associates with the dimeric adaptor proteins in a folded conformation of the kinase domain. The similarity of this structure with the B-RAF/14-3-3 complex (Kondo et al., 2019) and the phosphorylation sites found in the isolated RHC complex suggest that the assembly of RAF1 with the HSP90-CDC37 system may facilitate the activating phosphorylation. Although the kinase domain will remain unfolded and therefore inactive, this conformation could facilitate its phosphorylation in the S259 and S621 residues. Consequently, the RHC complex will maintain RAF1 in a “ready-to-act pool.” Once the folding of the kinase domain is completed, the 14-3-3 proteins would associate with the phosphorylated RAF1 to regulate its further activation (Figures 7A and 7B). On a different level of regulation, heterodimerization between RAF1 with A-RAF or B-RAF has been shown to be a part of the physiological activation process, and the heterodimer displays distinct

biochemical properties likely to be important for signaling regulation (Rushworth et al., 2006) (Su et al., 2022; Venkatanarayan et al., 2022). We speculate that the interaction of RAF1 with the HSP90-CDC37 system could control the dynamics of the RAF1 heterodimers formed with the 14-3-3 proteins by providing folded and phosphorylated kinase, thus influencing the levels of homo or heterodimers of this signaling module and thereby influencing cellular proliferation (Figure 7B).

Limitations of the study

We can observe differences between the CDK4 and RAF1 complexes with HSP90-CDC37 related to the kinase domain structure. Yet, how these differences influence their folding efficiency is unclear. Our work also indicates that 14-3-3 proteins stabilize RAF1 after the kinase domain folding by HSP90-CDC37. However, the low resolution of the RAF1/14-3-3 complex does not allow us to determine whether the mechanism of RAF1 activation is similar to that recently reported for B-RAF (Kondo et al., 2019; Fiesco et al., 2022; Park et al., 2019). In addition, while the disruption of the RHC complex could be a therapeutic target due to degradation of RAF1, such strategies would need to conserve the HSP90-CDC37 chaperone homeostatic function to avoid undesired toxicity. Finally, the proliferation assays using “Rafless” MEFs do not allow us to determine the relative contributions of protein instability and lack of kinase activity due to the elevated levels of the ectopically expressed RAF1 mutant isoforms.

STAR★METHODS

Detailed methods are provided in the online version of this paper and include the following:

- KEY RESOURCES TABLE
- RESOURCE AVAILABILITY
 - Lead contact
 - Materials availability
 - Data and code availability
- EXPERIMENTAL MODEL AND SUBJECT DETAILS
 - Cell lines
- METHOD DETAILS
 - Plasmid preparation and expression in Expi293F mammalian cells
 - Purification of the RAF1-HSP90-CDC37 complex
 - Purification of 14-3-3 ζ
 - Cryo-EM sample preparation and data collection
 - Cryo-EM data processing
 - Model building and refinement
 - Western blot analysis and antibodies
 - Protein kinase assay
 - Sample preparation for mass spectrometry and size-exclusion chromatography with multiangle light scattering (SEC-MALS) analysis
 - Size-exclusion chromatography with multiangle light scattering (SEC-MALS) analysis
 - CDC37 purification and binding assays on cellulose-bound peptides containing RAF family sequences
 - Site-directed mutagenesis and pull-downs from cell lysates

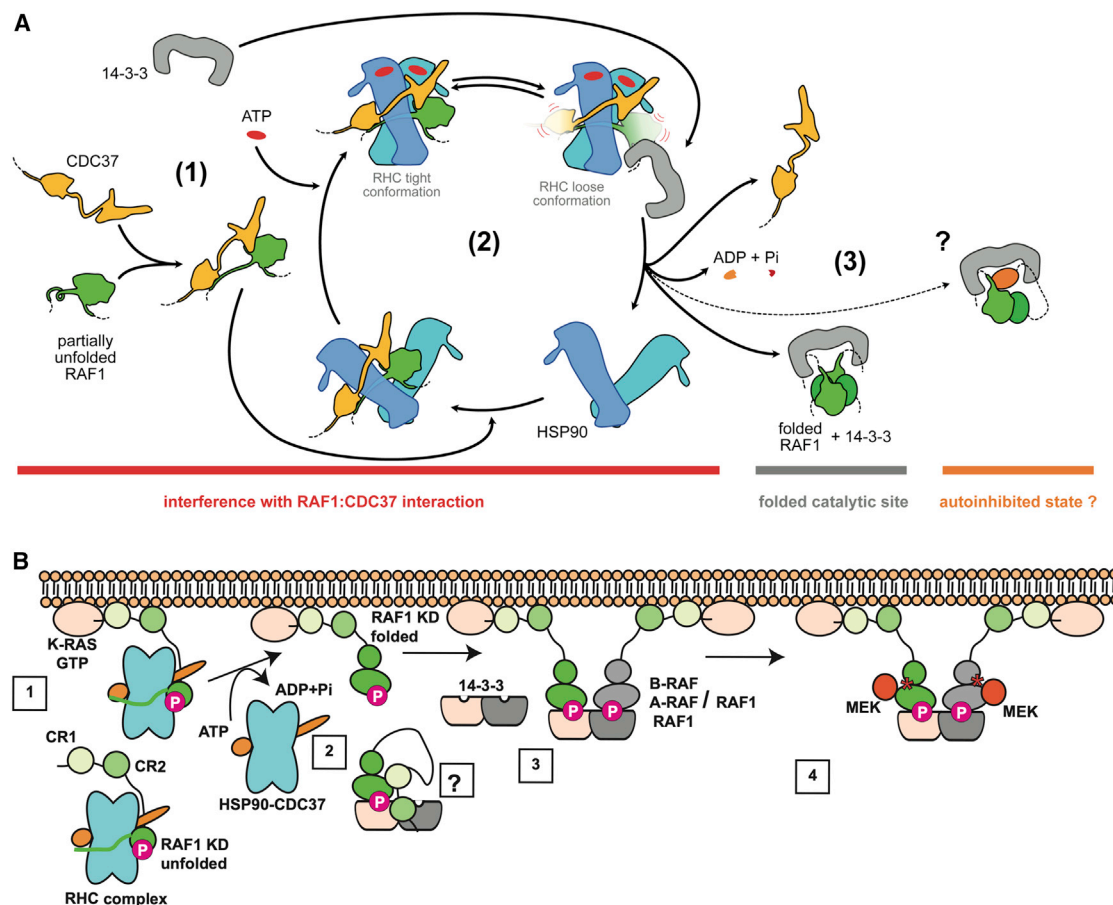


Figure 7. Model of RAF1 folding by the HSP90-CDC37 chaperone system and RHC function within the RAF1 regulation

(A) The unfolded RAF1 protein associates to CDC37 and is stabilized after assembly with HSP90 forming the RHC (1). The RHC displays a large conformational heterogeneity to stabilize the unfolded kinase and proceeds to fold RAF1 coupling the conformational changes with the hydrolysis of ATP (2). The folded RAF1 can interact with 14-3-3 proteins through S259 and S621 (3).

(B) RAF1 is stabilized by the HSP90-CDC37 complex (1). After interaction with KRAS in the GTP bound state and the hydrolysis of ATP by HSP90, the kinase domain of RAF1 is folded and S259 and S621 are phosphorylated (2). The folded and phosphorylated kinase binds 14-3-3 proteins. By analogy with B-RAF, RAF1 might present an autoinhibited state which could be released upon interaction with RAS (?). This has not been observed. Once folded, the second site of 14-3-3 could be occupied with another RAF kinase, either RAF1, A-RAF, or B-RAF (3). The hetero or homodimer is activated (asterisk) modulating the activity and the phosphorylation of MEK depending on the assembly of RAF homo or heterodimers (4). Therefore, the downstream signaling will be controlled by the ratio of folded RAF1 available, determining the proportion between homo and heterodimers, as wild-type B-RAF activity is not assisted by the HSP90-CDC37 system.

- Processing and analysis of mass spectrometry data
- Colony assay in *Rasless* and *Rafless* MEFs
- **QUANTIFICATION AND STATISTICAL ANALYSIS**

SUPPLEMENTAL INFORMATION

Supplemental information can be found online at <https://doi.org/10.1016/j.molcel.2022.08.012>.

ACKNOWLEDGMENTS

We thank the Danish Cryo-EM National Facility in CFIM at the University of Copenhagen for support during cryo-EM data collection. We also thank the Protein Expression Unit at CPR for assistance in protein expression and purification. S.G.-A. is a recipient of a postdoctoral fellowship from the Spanish Association against Cancer Scientific Foundation (FCAECC). This work was supported by grants from the European Research Council (ERC-2015-AdG/

695566, THERACAN), the Spanish Ministry of Science, Innovation and Universities (RTC-2017-6576-1), the Autonomous Community of Madrid (B2017/BMD-3884 iLUNG-CM), the CRIS Cancer Foundation, and the AECC (GC16173694BARB) to M.B. and by a grant from the Spanish Ministry of Science, Innovation and Universities (RTI2018-094664-B-I00) to M.B. and M.M.; M.B. is a recipient of an Endowed Chair from the AXA Research Fund. The Experimental Oncology group is a member of CIBERONC. G.M. is part of the Novo Nordisk Foundation Center for Protein Research (CPR), which is supported financially by the Novo Nordisk Foundation (grant NNF14CC0001). This work was also supported by grant NNF0024386, grant NNF17SA0030214, and Distinguished Investigator grant NNF18OC0055061 to G.M., who is a member of the Integrative Structural Biology Cluster (ISBUC) at the University of Copenhagen.

AUTHOR CONTRIBUTIONS

M.B. and G.M. conceived the study. S.G.-A., M.B., and G.M. designed the biochemical experiments. S.G.-A. and J.M.-T. set up the purification protocol.

S.G.-A., L.d.I.P.O., and G.A. created the mutants and performed biochemistry experiments. S.G.-A. and C.G.L. performed tissue culture experiments. E.Z. and J.M. performed mass spectrometry analysis and analyzed the results. C.M.S. and R.C.-O. performed the SEC-MALS analysis. P.M. prepared EM grids and collected the cryo-EM images. P.M. performed cryo-EM data processing and built the models structure, and P.M. and G.M. proceeded with cryo-EM map and structure analysis. The global results were discussed and evaluated with all authors. G.M. and M.B. coordinated and supervised the project and wrote the manuscript with input from all of the authors.

DECLARATION OF INTERESTS

Guillermo Montoya is a co-founder and member of the BoD of Twelve Bio.

Received: April 7, 2022

Revised: June 21, 2022

Accepted: August 8, 2022

Published: September 1, 2022

REFERENCES

- Adams, P.D., Afonine, P.V., Bunkóczi, G., Chen, V.B., Davis, I.W., Echols, N., Headd, J.J., Hung, L.W., Kapral, G.J., Grosse-Kunstleve, R.W., et al. (2010). Phenix: a comprehensive Python-based system for macromolecular structure solution. *Acta Crystallogr. D Biol. Crystallogr.* **66**, 213–221.
- Asanow, D., Palovcak, E., and Cheng, Y. (2019). asanow/pyem: UCSF pyem v0.5 (v0.5). Zenodo. <https://doi.org/10.5281/zenodo.3576630>.
- Blasco, M.T., Navas, C., Martin-Serrano, G., Grana-Castro, O., Lechuga, C.G., Martin-Diaz, L., Djurec, M., Li, J., Morales-Cacho, L., Esteban-Burgos, L., et al. (2019). Complete regression of advanced pancreatic ductal adenocarcinomas upon combined inhibition of EGFR and C-RAF. *Cancer Cell* **35**, 573–587.e6.
- Croll, T.I. (2018). ISOLDE: a physically realistic environment for model building into low-resolution electron-density maps. *Acta Crystallogr. D Struct. Biol.* **74**, 519–530.
- Diedrich, B., Rigbolt, K.T., Röring, M., Herr, R., Kaeser-Pebarnard, S., Gretzmeier, C., Murphy, R.F., Brummer, T., and Dengjel, J. (2017). Discrete cytosolic macromolecular BRAF complexes exhibit distinct activities and composition. *EMBO J.* **36**, 646–663.
- Drosten, M., Dhawahir, A., Sum, E.Y., Urosevic, J., Lechuga, C.G., Esteban, L.M., Castellano, E., Guerra, C., Santos, E., and Barbacid, M. (2010). Genetic analysis of Ras signalling pathways in cell proliferation, migration and survival. *EMBO J.* **29**, 1091–1104.
- Emsley, P., Lohkamp, B., Scott, W.G., and Cowtan, K. (2010). Features and development of coot. *Acta Crystallogr. D Biol. Crystallogr.* **66**, 486–501.
- García-Cardeña, G., Fan, R., Shah, V., Sorrentino, R., Cirino, G., Papapetropoulos, A., and Sessa, W.C. (1998). Dynamic activation of endothelial nitric oxide synthase by Hsp90. *Nature* **392**, 821–824. <https://doi.org/10.1038/33934>.
- Genest, O., Reidy, M., Street, T.O., Hoskins, J.R., Camberg, J.L., Agard, D.A., Masison, D.C., and Wickner, S. (2013). Uncovering a region of heat shock protein 90 important for client binding in *E. coli* and chaperone function in yeast. *Mol. Cell* **49**, 464–473.
- Goddard, T.D., Huang, C.C., Meng, E.C., Pettersen, E.F., Couch, G.S., Morris, J.H., and Ferrin, T.E. (2018). UCSF ChimeraX: meeting modern challenges in visualization and analysis. *Protein Sci.* **27**, 14–25.
- Grammatikakis, N., Lin, J.H., Grammatikakis, A., Tschlis, P.N., and Cochran, B.H. (1999). p50(cdc37) acting in concert with Hsp90 is required for Raf-1 function. *Mol. Cell. Biol.* **19**, 1661–1672.
- Grant, T., Rohou, A., and Grigorieff, N. (2018). cisTEM, user-friendly software for single-particle image processing. *eLife* **7**, e35383.
- Grbovic, O.M., Basso, A.D., Sawai, A., Ye, Q., Friedlander, P., Solit, D., and Rosen, N. (2006). V600E B-Raf requires the Hsp90 chaperone for stability and is degraded in response to Hsp90 inhibitors. *Proc. Natl. Acad. Sci. USA* **103**, 57–62.
- Hartson, S.D., Thulasiraman, V., Huang, W., Whitesell, L., and Matts, R.L. (1999). Molybdate inhibits hsp90, induces structural changes in its C-terminal domain, and alters its interactions with substrates. *Biochemistry* **38**, 3837–3849.
- Keramisanou, D., Aboalroub, A., Zhang, Z., Liu, W., Marshall, D., Diviney, A., Larsen, R.W., Landgraf, R., and Gelis, I. (2016). Molecular mechanism of protein kinase recognition and sorting by the Hsp90 kinome-specific cochaperone Cdc37. *Mol. Cell* **62**, 260–271.
- Kidmose, R.T., Juhl, J., Nissen, P., Boesen, T., Karlsen, J.L., and Pedersen, B.P. (2019). Namdinator - automatic molecular dynamics flexible fitting of structural models into cryo-EM and crystallography experimental maps. *IUCrJ* **6**, 526–531.
- Kondo, Y., Ognjenović, J., Banerjee, S., Karandur, D., Merk, A., Kulhanek, K., Wong, K., Roose, J.P., Subramaniam, S., and Kuriyan, J. (2019). Cryo-EM structure of a dimeric B-Raf:14-3-3 complex reveals asymmetry in the active sites of B-Raf kinases. *Science* **366**, 109–115.
- Lavery, L.A., Partridge, J.R., Ramelot, T.A., Elnatan, D., Kennedy, M.A., and Agard, D.A. (2014). Structural asymmetry in the closed state of mitochondrial Hsp90 (TRAP1) supports a two-step ATP hydrolysis mechanism. *Mol. Cell* **53**, 330–343.
- Lechuga, C.G., Salmón, M., Paniagua, G., Guerra, C., Barbacid, M., and Drosten, M. (2021). RASless MEFs as a tool to study RAS-dependent and RAS-independent functions. *Methods Mol. Biol.* **2262**, 335–346.
- Maloney, R.C., Zhang, M., Jang, H., and Nussinov, R. (2021). The mechanism of activation of monomeric B-Raf V600E. *Comput. Struct. Biotechnol. J.* **19**, 3349–3363.
- Martín, A., Odajima, J., Hunt, S.L., Dubus, P., Ortega, S., Malumbres, M., and Barbacid, M. (2005). Cdk2 is dispensable for cell cycle inhibition and tumor suppression mediated by p27(Kip1) and p21(Cip1). *Cancer Cell* **7**, 591–598.
- Martinez Fiesco, J.A., Durrant, D.E., Morrison, D.K., and Zhang, P. (2022). Structural insights into the BRAF monomer-to-dimer transition mediated by RAS binding. *Nat. Commun.* **13**, 486.
- Matallanas, D., Birtwistle, M., Romano, D., Zebisch, A., Rauch, J., von Kriegsheim, A., and Kolch, W. (2011). Raf family kinases: old dogs have learned new tricks. *Genes Cancer* **2**, 232–260.
- Mikula, M., Schreiber, M., Husak, Z., Kucerova, L., Rütth, J., Wieser, R., Zatloukal, K., Beug, H., Wagner, E.F., and Baccarini, M. (2001). Embryonic lethality and fetal liver apoptosis in mice lacking the c-raf-1 gene. *EMBO J.* **20**, 1952–1962.
- Mitra, S., Ghosh, B., Gayen, N., Roy, J., and Mandal, A.K. (2016). Bipartite role of heat shock Protein 90 (Hsp90) keeps CRAF kinase poised for activation. *J. Biol. Chem.* **291**, 24579–24593.
- Morrison, D.K., and Cutler, R.E. (1997). The complexity of Raf-1 regulation. *Curr. Opin. Cell Biol.* **9**, 174–179.
- Noble, C., Mercer, K., Hussain, J., Carragher, L., Giblett, S., Hayward, R., Patterson, C., Marais, R., and Pritchard, C.A. (2008). CRAF autophosphorylation of serine 621 is required to prevent its proteasome-mediated degradation. *Mol. Cell* **31**, 862–872.
- Park, E., Rawson, S., Li, K., Kim, B.W., Ficarro, S.B., Pino, G.G., Sharif, H., Marto, J.A., Jeon, H., and Eck, M.J. (2019). Architecture of autoinhibited and active BRAF-MEK1-14-3-3 complexes. *Nature* **575**, 545–550.
- Prince, T., and Matts, R.L. (2004). Definition of protein kinase sequence motifs that trigger high affinity binding of Hsp90 and Cdc37. *J. Biol. Chem.* **279**, 39975–39981.
- Punjani, A., and Fleet, D.J. (2021). 3D variability analysis: resolving continuous flexibility and discrete heterogeneity from single particle cryo-EM. *J. Struct. Biol.* **213**, 107702.
- Punjani, A., Rubinstein, J.L., Fleet, D.J., and Brubaker, M.A. (2017). cryoSPARC: algorithms for rapid unsupervised cryo-EM structure determination. *Nat. Methods* **14**, 290–296.
- Rohou, A., and Grigorieff, N. (2015). CTFFIND4: fast and accurate defocus estimation from electron micrographs. *J. Struct. Biol.* **192**, 216–221.

- Roskoski, R., and Jr. (2010). RAF protein-serine/threonine kinases: structure and regulation. *Biochem. Biophys. Res. Commun.* **399**, 313–317.
- Rushworth, L.K., Hindley, A.D., O'Neill, E., and Kolch, W. (2006). Regulation and role of Raf-1/B-Raf heterodimerization. *Mol. Cell. Biol.* **26**, 2262–2272.
- SanClemente, M., Francoz, S., Esteban-Burgos, L., Bousquet-Mur, E., Djurec, M., Lopez-Casas, P.P., Hidalgo, M., Guerra, C., Drosten, M., Musteanu, M., and Barbacid, M. (2018). c-RAF ablation induces regression of advanced Kras/Trp53 mutant lung adenocarcinomas by a mechanism independent of MAPK signaling. *Cancer Cell* **33**, 217–228.e4.
- SanClemente, M., Nieto, P., Garcia-Alonso, S., Fernández-García, F., Esteban-Burgos, L., Guerra, C., Drosten, M., Caleiras, E., Martínez-Torrecuadrada, J., Santamaría, D., et al. (2021). RAF1 kinase activity is dispensable for KRAS/p53 mutant lung tumor progression. *Cancer Cell* **39**, 294–296.
- Scheres, S.H. (2012). RELION: implementation of a Bayesian approach to cryo-EM structure determination. *J Struct Biol.* **180**, 519–530. <https://doi.org/10.1016/j.jsb.2012.09.006>.
- Schneider, C.A., Rasband, W.S., and Eliceiri, K.W. (2012). NIH Image to ImageJ: 25 years of image analysis. *Nat. Methods* **9**, 671–675.
- Schopf, F.H., Biebl, M.M., and Buchner, J. (2017). The HSP90 chaperone machinery. *Nat. Rev. Mol. Cell Biol.* **18**, 345–360.
- Su, W., Mukherjee, R., Yaeger, R., Son, J., Xu, J., Na, N., Merna Timaul, N., Hechtman, J., Paroder, V., Lin, M., et al. (2022). ARAF protein kinase activates RAS by antagonizing its binding to rasgap NF1. *Mol. Cell* **82**, 2443–2457.e7.
- Taipale, M., Krykbaeva, I., Koeva, M., Kayatekin, C., Westover, K.D., Karras, G.I., and Lindquist, S. (2012). Quantitative analysis of HSP90-client interactions reveals principles of substrate recognition. *Cell* **150**, 987–1001.
- Tan, Y.Z., Baldwin, P.R., Davis, J.H., Williamson, J.R., Potter, C.S., Carragher, B., and Lyumkis, D. (2017). Addressing preferred specimen orientation in single-particle cryo-EM through tilting. *Nat Methods* **14**, 793–796. <https://doi.org/10.1038/nmeth.4347>.
- Terasawa, K., Yoshimatsu, K., Iemura, S., Natsume, T., Tanaka, K., and Minami, Y. (2006). Cdc37 interacts with the glycine-rich loop of Hsp90 client kinases. *Mol. Cell. Biol.* **26**, 3378–3389.
- Tunyasuvunakool, K., Adler, J., Wu, Z., Green, T., Zielinski, M., Židek, A., Bridgland, A., Cowie, A., Meyer, C., Laydon, A., et al. (2021). Highly accurate protein structure prediction for the human proteome. *Nature* **596**, 590–596.
- Vaughan, C.K., Mollapour, M., Smith, J.R., Truman, A., Hu, B., Good, V.M., Panaretou, B., Neckers, L., Clarke, P.A., Workman, P., et al. (2008). Hsp90-dependent activation of protein kinases is regulated by chaperone-targeted dephosphorylation of Cdc37. *Mol. Cell* **31**, 886–895.
- Venkatarayanan, A., Liang, J., Yen, I., Shanahan, F., Haley, B., Phu, L., Verschuere, E., Hinkle, T.B., Kan, D., Segal, E., et al. (2022). CRAF dimerization with ARAF regulates KRAS-driven tumor growth. *Cell Rep.* **38**, 110351.
- Verba, K.A., Wang, R.Y., Arakawa, A., Liu, Y., Shirouzu, M., Yokoyama, S., and Agard, D.A. (2016). Atomic structure of Hsp90-Cdc37-Cdk4 reveals that Hsp90 traps and stabilizes an unfolded kinase. *Science* **352**, 1542–1547.
- Wartmann, M., and Davis, R.J. (1994). The native structure of the activated Raf protein kinase is a membrane-bound multi-subunit complex. *J. Biol. Chem.* **269**, 6695–6701.
- Zheng, S.Q., Palovcak, E., Armache, J.P., Verba, K.A., Cheng, Y., and Agard, D.A. (2017). MotionCor2: anisotropic correction of beam-induced motion for improved cryo-electron microscopy. *Nat. Methods* **14**, 331–332.
- Zhong, E.D., Bepler, T., Berger, B., and Davis, J.H. (2021). CryoDRGN: reconstruction of heterogeneous cryo-EM structures using neural networks. *Nat. Methods* **18**, 176–185.
- Zivanov, J., Nakane, T., and Scheres, S.H.W. (2020). Estimation of high-order aberrations and anisotropic magnification from cryo-EM data sets in RELION-3.1. *IUCr J* **7**, 253–267.

STAR★METHODS

KEY RESOURCES TABLE

REAGENT or RESOURCE	SOURCE	IDENTIFIER
Antibodies		
Mouse monoclonal anti-HSP90 α/β (F8)	Santa Cruz Biotechnology	Cat# sc-13119; RRID: AB_675659
Mouse monoclonal anti-c-Raf-1	BD	Cat# 610151; RRID: AB_397552
Mouse monoclonal anti-Cdc37 (E-4)	Santa Cruz Biotechnology	Cat# sc-13129; AB_627232
Mouse monoclonal anti-14-3-3 ϵ (F-3)	Santa Cruz Biotechnology	Cat# sc-393177
Mouse monoclonal anti-14-3-3 ζ (1B3)	Santa Cruz Biotechnology	Cat# sc-293415
Rabbit polyclonal anti-A-Raf	Cell Signaling	Cat# 4432; RRID: AB_330813
Mouse monoclonal anti-Raf-B (F-7)	Santa Cruz Biotechnology	Cat# sc-5284; RRID: AB_626760
Rabbit polyclonal anti-phospho-MEK1/2 (Ser217/221)	Cell Signaling	Cat# 9121; RRID: AB_331648
Mouse monoclonal anti-Pan-Ras (clone RAS 10)	Calbiochem	Cat# OP40; RRID: AB_10683383
Mouse monoclonal anti-Vinculin (clone hVIN-1)	Sigma-Aldrich	Cat# V9131; RRID: AB_477629
Chemicals, peptides, and recombinant proteins		
4-hydroxy-Tamoxifen	Sigma	Cat# H7904
Puromycin	InvivoGen	Cat# ant-pr-1
Blasticidin	EDM Millipore Corp	Cat# 203350
Phosphatase Inhibitor Cocktail 2	Sigma	Cat# P5726
Phosphatase Inhibitor Cocktail 3	Sigma	Cat# P0044
cComplete Mini	Roche	Cat# 11836153001
Bradford	Bio-Rad	Cat# 500-0006
HindIII enzyme	New England Biolabs	Cat# R0140S
XhoI enzyme	New England Biolabs	Cat# R0146S
Desthiobiotin	Iba	Cat# 2-1000-005
MES	Sigma-Aldrich	Cat# M0164
Na ₂ MoO ₄	Sigma-Aldrich	Cat# 7631-95-0
TCEP, Hydrochloride, Reagent Grade	Calbiochem	Cat# 51805-45-9
Trypsin Gold, Mass Spectrometry Grade	Promega	Cat# V528A
Lysyl Endopeptidase®, Mass Spectrometry Grade (Lys-C)	Wako	Cat# 121-05063
Pierce™ C ₁₈ stage-tips	ThermoFisher Scientific	Cat# 87782
Cellulose- β alanine-membrane with overlapping dodecapeptides (custom)	JPT	N/A
TAT-peptides (custom)	GenScript	N/A
Thiazolyl Blue Tetrazolium Bromide (MTT)	Sigma Aldrich	Cat# M5655
Critical commercial assays		
ExpiFectamine™ 293 Transfection Kit	ThermoFisher Scientific	Cat# A14524
In-Fusion® HD EcoDry™ Cloning Kit	Takara Biol USA	Cat# 639690
RAF1 Kinase Assay Kit	Sigma Aldrich	Cat#14-352; Cat# 14-420; Cat# 20-113; Cat# 20-108; Cat# 07-461
QuickChange Lightning Site-Directed Mutagenesis Kit	Agilent Technologies	Cat# 210519
Deposited data		
Map of RHC-I	This paper	EMD-14473

(Continued on next page)

Continued

REAGENT or RESOURCE	SOURCE	IDENTIFIER
Model of RHC-I	This paper	PDB: 7Z38
Map of RHC-II	This paper	EMD-14472
Model of RHC-II	This paper	PDB: 7Z37
Experimental models: Cell lines		
Mouse Embryonic Fibroblast: <i>H-Ras</i> ^{-/-} ; <i>N-Ras</i> ^{-/-} ; <i>K-Ras</i> ^{lox/lox} (K-Raslox)	Laboratory of Mariano Barbacid	N/A
Mouse Embryonic Fibroblast: A-Raf ^{lox/lox} , B-Raf ^{lox/lox} ; Raf1 ^{lox/lox} (Raflox)	Laboratory of Mariano Barbacid	N/A
Human: Expi293F™ cells	ThermoFisher Scientific	Cat# A14527
Oligonucleotides		
DNA primers	This paper	Table S4
Recombinant DNA		
pcDNA™3.1(+) Mammalian Expression Vector	Invitrogen	Cat# V79020
Plasmid: pcDNA3-RAF1-Strep	This paper	N/A
Human HSP90: pcDNA3-HSP90-HA	García-Cardeña et al., 1998	Addgene Plasmid #22487
CDC37 (NM_007065) Human Tagged ORF Clone	Origene	Cat# RC201002
Plasmid: pcDNA3-CDC37-Strep	This paper	N/A
Plasmid: pcDNA3-CDC337_I23E-Strep	This paper	N/A
Plasmid: pcDNA3-RAF1_L459E-Strep	This paper	N/A
Plasmid: pcDNA3-RAF1_I464E-Strep	This paper	N/A
Plasmid: pcDNA3-RAF1_K483A-Strep	This paper	N/A
Plasmid: pcDNA3-RAF1_I484A-Strep	This paper	N/A
Plasmid: pcDNA3-RAF1_D486A-Strep	This paper	N/A
Plasmid: pcDNA3-RAF1_F487A-Strep	This paper	N/A
Plasmid: pcDNA3-RAF1_F487R-Strep	This paper	N/A
Plasmid: pBABE-puro-Raf1-WT-CAAX	This paper	N/A
Plasmid: pBABE-puro-Raf1-D486A-CAAX	This paper	N/A
Plasmid: pBABE-puro-Raf1-F487A-CAAX	This paper	N/A
Plasmid: pBABE-puro-Raf1-D486A/F487A-CAAX	This paper	N/A
Plasmid: pLVX-RAF1_WT-Strep	This paper	N/A
Plasmid: pLVX-RAF1_D486A-Strep	This paper	N/A
Plasmid: pLVX-RAF1_F487A-Strep	This paper	N/A
Plasmid: pLVX-RAF1_D486A/F487A-Strep	This paper	N/A
Plasmid: pRetroSuper-shRHA-p16 ^{INK4a}	Drosten et al., 2010	N/A
Plasmid pET21d-14-3-3	This paper	N/A
Software and algorithms		
Graphpad Prism 5.01	N/A	N/A
ImageJ	Schneider et al., 2012	https://imagej.nih.gov/ij/
ASTRA6	Wyatt Technology	https://wyatt-technology-astra.software.informer.com/versions/
RELION 3.13	Scheres, 2012	https://relion.readthedocs.io/en/release-3.1/
cisTEM 1.0.0	Grant et al., 2018	https://cistem.org/
cryoSPARC 3.3.1	Punjani et al., 2017	https://cryosparc.com/docs
MotionCor2	Zheng et al., 2017	https://emcore.ucsf.edu/ucsf-software

(Continued on next page)

Continued

REAGENT or RESOURCE	SOURCE	IDENTIFIER
CTFFIND4	Rohou and Grigorieff, 2015	https://grigoriefflab.umassmed.edu/ctffind4
pyEM	Asarnow et al., 2019	https://doi.org/10.5281/zenodo.3576630
cryoDRGN	Zhong et al., 2021	http://cb.csail.mit.edu/cb/cryodrgn/
Phenix	Adams et al., 2010; Adams et al., 2010	http://www.phenix-online.org/
COOT	Emsley et al., 2010	https://www2.mrc-lmb.cam.ac.uk/personal/pemsley/coot/
Naminator	Kidmose et al., 2019	https://naminator.au.dk/
AlphaFold v2.0	Tunyasuvunakool et al., 2021	https://github.com/deepmind/alphafold
3DFSC	Tan et al., 2017	https://3dfsc.salk.edu/
ChimeraX	Goddard et al., 2018	https://www.cgl.ucsf.edu/chimerax/
PyMOL	The PyMOL Molecular Graphics System, Version 2.0 Schrödinger, LLC.	http://www.pymol.org/2/

Other

NUPAGE™ 4-12% Bis-Tris Midi Gel	Invitrogen	Cat# WG1402
Nitrocellulose Blotting Membrane	GE Healthcare	Cat# 10600001
ECL Prime Western Blotting Detection Reagent	GE Healthcare	Cat# 28980926
Superdex 200 Increase 10/300 GL	Cytiva Life Sciences	Cat# 28990944
HiLoad 16/600 Superdex 200 pg	Cytiva Life Sciences	Cat# 28989335
StrepTrap HP column 5 mL	Cytiva Life Sciences	Cat# 28907548
StrepTactin™ Sepharose® High Performance	Cytiva Life Sciences	Cat# 28935600
ÄKTApurify	Cytiva Life Sciences	Cat# 28908936
Expi293™ Expression Medium - Gibco	ThermoFisher Scientific	Cat# A1435101
Opti-MEM™ I Reduced Serum Medium, GlutaMAX™ Supplement - Gibco	ThermoFisher Scientific	Cat# 51985026
Cryo-EM grids 200 mesh R 2/2 UltrAuFoil	Quantifoil	https://www.quantifoil.com/products/ultrafoil/

RESOURCE AVAILABILITY

Lead contact

Further information and requests for resources and reagents should be directed to and will be fulfilled by the lead contact, Guillermo Montoya (guillermo.montoya@cpr.ku.dk).

Materials availability

All reagents generated in this study are available upon request to the [lead contact](#) with a completed Materials Transfer Agreement.

Data and code availability

- The atomic coordinates and cryo-EM maps included in this study have been deposited in the Protein Data Bank and Electron Microscopy Data Bank under the accession codes: RHC-I, PDB:7Z38 and EMDB:14473; RHC-II, PDB:7Z37 and EMDB:14472.
- This paper does not report original code.
- Any additional information required to reanalyze the data reported in this paper is available from the [lead contact](#) upon request.

EXPERIMENTAL MODEL AND SUBJECT DETAILS

Cell lines

“K-Raslox” and “Raflox” Mouse Embryonic Fibroblast (MEF) cell lines were generated at Barbacid Laboratory. Cells were cultured in DMEM (Gibco) supplemented with 10% FBS (Gibco) at 37 °C and 5% CO₂ in a humidified incubator. Cells were suspended using Trypsin-EDTA solution (Gibco) and split every 2 to 3 days.

METHOD DETAILS

Plasmid preparation and expression in Expi293F mammalian cells

The human full-length RAF1 cDNA (accession number NM_002880.3) was amplified by PCR with restriction site-tailed primers incorporating a C-terminal StrepTagII, separated from the protein by a Gly-Ser-Ala residue linker. The resulting DNA was cloned into the HindIII/XhoI sites of the transfer vector pcDNA3 (Invitrogen), using the In-Fusion® HD EcoDry Cloning Kit (Takara Bio USA). The derivative plasmid, pcDNA3-RAF1-Strep, was sequence verified. The plasmid encoding the full-length human HSP90 beta with a HA-tag at its N terminus was obtained from Addgene (Plasmid #22487). The cDNA clone for full-length human CDC37 tagged with a C-terminal Myc-DDK tag was purchased from Origene (RC201002). Expi293F cells (ThermoFisher Scientific) were maintained and expanded following the recommendations of the manufacturer. In short, Expi293F cells were grown in Expi293 Expression Medium (ThermoFisher Scientific) at 37 °C, 120 rpm, 5% CO₂ atmosphere in PETG Erlenmeyer flasks with 0.2 μm ventilated caps (Corning) and split roughly every fourth day. Transfection of cells were performed with ExpiFectamine 293 Transfection Kit, following the manufacturer's recommendations. For each transfection, cells were diluted to a final density of 3 mvc/ml in a total volume of 120 ml (in a 500 ml flask) and transfected with a total of 120 μg of plasmid DNA (56 μg of pcDNA3-RAF1-Strep + 32 μg of pcDNA3-HSP90-HA + 32 μg of pCMV6-CDC37-Myc-DDK), diluted with OptiMEM I-GlutaMAX (ThermoFisher Scientific). Cells were allowed to growth in standard conditions for 48 additional hours and then were harvested.

Purification of the RAF1-HSP90-CDC37 complex

Four batches of transfected Expi293F cells (480 ml total) were resuspended individually in 15 ml of lysis buffer (20 mM Tris-HCl [pH 7.5], 150 mM NaCl, 10 mM MgCl₂, 10 mM KCl, 20 mM Na₂MoO₄ and 0.1% Triton X-100) supplemented with complete Mini Protease Inhibitor Cocktail (Merck) and Phosphatase Inhibitor Cocktails 2 and 3 (Merk) and left on agitation at 4 °C for 15 minutes. After a brief sonication, the lysate was centrifuged (10,000 rpm, 10 min, 4 °C) and the soluble fraction was purified by affinity chromatography using a 5-ml StrepTrap® column (GE Healthcare), on an ÄKTA prime (GE Healthcare). The StrepTrap column was washed with 20 column volumes (CV) of buffer A1 (20 mM Tris-HCl [pH 7.5], 150 mM NaCl, 10 mM MgCl₂, 10 mM KCl, 20 mM Na₂MoO₄) and eluted with a stepwise gradient (0–100%) of buffer B1 (20 mM Tris-HCl [pH 7.5], 150 mM NaCl, 10 mM MgCl₂, 10 mM KCl, 20 mM Na₂MoO₄ and 2.5 mM desthiobiotin). RAF1-containing fractions were pooled, concentrated to <5 ml with a 30-kDa Vivaspin concentrator (Sartorius), and further purified by size exclusion chromatography (SEC) with a Superdex S200 16/600 column (GE Healthcare) in buffer A1, using an ÄKTA FPLC system (GE Healthcare). Protein standards (Gel Filtration Calibration Kit, GE Healthcare) were loaded onto the column for molecular weight calibration using the same method. Finally, the eluted peak corresponding to RAF1-CDC37-HSP90 complexes was collected and concentrated with a 30-kDa Vivaspin concentrator to final concentration of about 2 mg/ml and stored at -80°C until use.

Purification of 14-3-3ζ

The expression plasmid pET21d-14-3-3ζ-HisTag was transformed into *Escherichia coli* BL21(DE3) CodonPlus competent cells. The cells were incubated in Terrific Broth medium with 30 μg/ml ampicillin and 34 μg/ml chloramphenicol at 37°C until the OD 600 reached 1.0. The temperature was then changed to 20°C and the *E. Coli* cells were incubated for a further 1 h. Protein expression was induced by isopropyl β-D-1-thiogalactopyranoside at a final concentration of 0.25 mM for 18 h. The *E. Coli* cells were collected by centrifugation at 6,000 g for 10 min and suspended in six times the volume of lysis buffer consisting of 20 mM HEPES-Na pH 7.5, 500 mM NaCl, 5% glycerol, 20 mM imidazole, 5 mM β-mercaptoethanol, 1 mM phenylmethylsulfonyl fluoride; the cells were then broken by a high-pressure homogenizer at 80 Mpa. Cell debris was removed by centrifugation for 40 min at 20,000 g. The supernatant was mixed with 3 ml Ni Sepharose (GE Healthcare) for 1 h and the beads were then sequentially washed with ten times volume of lysis buffer containing 20 and 40 mM imidazole. The protein was eluted with five times the volume of lysis buffer plus 300 mM imidazole. The protein was concentrated and loaded onto a HiLoad 16/60 Superdex 200 pg column (GE Healthcare) pre-equilibrated with 20 mM HEPES-Na pH 7.5, 100 mM NaCl, 1 mM DTT. Finally, the eluted peak corresponding to 14-3-3ζ was collected with a 10-kDa Vivaspin concentrator to final concentration of about 5.3 mg/ml and stored at -80°C until use.

Cryo-EM sample preparation and data collection

For Cryo-EM, fresh RHC fractions from the Superdex S200, at a concentration of 0.6 mg/ml, were flash frozen in liquid nitrogen and stored at -80°C. Initially, the RHC samples were diluted with buffer A1 to a final concentration of 0.3 mg/ml for cryo-EM grid preparation, data collection and processing. Analysis of these initial results showed a strong preferential orientation of the RHC complexes in the grids. To alleviate the associated anisotropy in the obtained maps, additional tilted images (30°) were also collected as default protocol (Figure S2F). Furthermore, we observed that the large heterogeneity of the RHC complexes, with a relatively small fraction of the particles yielding medium to high resolution maps, could be reduced when adding the 14-3-3 protein to the sample, improving the 3D classifications and reconstructions of the complex. Final grids were prepared incubating the RHC complex (0.3 mg/ml final concentration in buffer A1) with the 14-3-3 protein (1:2.5 mole ratio, RHC:14-3-3ζ) 20 minutes in ice. A volume of 3 μl was applied to glow-discharged grids (Quantifoil R2/2 200 mesh Au grids; Leica EM ACE200, 50 s at 5 mA) and frozen using a Vitrobot Mark IV (FEI, Thermo Fisher Scientific; settings: 100% humidity, 277K and blot time 3 s). Grids were screened on a Glacios TEM (Thermo Fisher Scientific) and the best grid was transferred to a Titan Krios microscope (Thermo Fisher Scientific) operating at

300 kV at liquid nitrogen temperature. Dose-fractionated Movies (8138 in total: 4430 non-tilted and 3708 30° tilted; Figure S3A) were recorded using a Falcon 3EC Direct Electron Detector (Thermo Fisher Scientific) in electron counting mode (30 frames/Movie, with a dose rate of $\sim 1 \text{ e}^-/\text{\AA}^2$ per frame, a defocus range of -0.5 to $-2.5 \mu\text{m}$ and a pixel size of $0.832 \text{ \AA}/\text{pixel}$).

Cryo-EM data processing

The data from initial experiments were processed using cisTEM (Grant et al., 2018) and Relion (Zivanov et al., 2020), using in the pre-processing steps MotionCor2 (Zheng et al., 2017) and CTFFIND4 (Rohou and Grigorieff, 2015). For the final data, obtained from the sample including 14-3-3, all the pre-processing was performed in cryoSPARC (Punjani et al., 2017) because of the convenience of its patch motion correction and patch CTF estimation protocols for the analysis of medium-small particles and tilted images. A summary of the steps in the image processing procedures is shown in Figure S3C. Coordinates of the particles were determined with the blob picker protocol (cryoSPARC) and a wide range of sizes were selected to cover from the large RHC complexes to the smaller 14-3-3 dimers (Figure S3B). A total of 3.7 million particles were extracted (Figure S3C) and subjected to successive 2D and 3D classifications (cryoSPARC), using as initial volumes the 3D reconstructions obtained with the *Ab-initio* protocol (cryoSPARC and later also within Relion) applied to different subsets of 2D classes.

RAF1:14-3-3 complex processing

Although the initial idea was to add 14-3-3 with the aim of isolate RHC:14-3-3 intermediate complexes, instead we discovered that only RAF1:14-3-3 complexes were obtained. Probably the binding of 14-3-3 to the CTD of RAF1 is too flexible and heterogeneous to be seen in the averaged 3D reconstructions, and maybe when the CTD peptides of RAF1 are fully accessible within the RHC complex the binding of 14-3-3 to them promotes the release of RAF1 from the HSP90 dimer. Accordingly, we classified the particles as RHC complexes (1.3 million particles), RAF1:14-3-3 complexes (1.2 million particles) and isolated 14-3-3 dimers (1.1 million particles). Although the processing was successfully continued inside cryoSPARC, extracted particles were imported, using pyEM (Asarnow et al., 2019), into Relion for the final refinements and reconstructions. After 2D/3D classification and refinements, only medium-resolution maps, around 6–7 Å, were obtained from the isolated 14-3-3 particles possibly because of their flexibility, relatively low density, and small size (Figure S3C). Similarly, just medium to low-resolution maps were produced after classification and auto/manual refinements of the particles categorized as [RAF1 dimer + 14-3-3 dimer] (Figures S3C and S7). In those particles, the 14-3-3 part seems to be located at different distances to the RAF1 dimer and with different relative orientations because of the flexibility of the RAF1 interacting CT peptides. Even with additional classifications, signal subtraction (14-3-3 region), masking and local refinement of exclusively the RAF1 dimer, high-resolution maps cannot be obtained apparently because of the high heterogeneity of the C-lobes, which connect directly to the 14-3-3 dimer through their bound CT peptides.

RHC complex processing

In the case of the RHC complex, three different approaches were followed to classify and characterize the 1353k RHC particles:

In a first approach 33 % of the initial particles can be classified into a 3D class that, although still highly heterogeneous, can produce a high-resolution map after 3D auto-refinement (RHC-0). The rest of the classes reflect a high degree of heterogeneity in all the components of the RHC complex, that prevents a proper refinement of the poses of the particles (Relion; Figure S3C). All these classes could represent intermediate states of the RHC complex where the HSP90 dimer is transitioning to more open conformations or different rearrangements of their different domains. As we are obtaining RAF1:14-3-3 complexes, probably empty HSP90 particles could be attracted to these inconclusive 3D classes. Analysis of the variability of the RHC-0 class using cryoSPARC (Punjani et al., 2017) and cryoDRGN (Zhong et al., 2021) showed that a large degree of flexibility, which is clearly localized at the RAF1 C-lobe and the visible regions of CDC37 (Figure 2) and that those two lateral blobs of the RHC complex behave independently, in an unconcerted manner. The high heterogeneity difficulted model building and hampered the generation of a high-resolution model.

A new 3D classification in Relion of the RHC-0 aiming for higher resolution yielded a map at 3.16 Å from 266k particles (RHC-I; Figures S4A–S4E and S5A). Local high resolution was achieved at this map, but clearly limited to the HSP90 dimer and the RAF1 extended segment that goes through it (Figures S4A and S4B); the corresponding regions to RAF1 C-lobe and CDC37 MD showed lower resolution and displayed their inherent not resolved heterogeneity, being not well defined. The use of tilted images helped in achieving a better distribution of orientations (Figures S3B–S3D) and reducing the anisotropy of the map (Figure S4E). In a second approach, a different set of classifications of the initial particles (Relion), now more focused in the characterization of the heterogeneity of RHC complex than trying to reach high-resolution, yielded eight different maps (Figures S3C and S5A). One of them, RHC-II shows the best defined RAF1 C-lobe and CDC37 MD, the latter containing an interacting portion of the RAF1 N-lobe (Figures 1E, 4D, S3C, and S5A). The RHC-II map presents similar characteristics than RHC-I, although the lower number of particles affect marginally its quality (local resolution, orientation distribution and anisotropy; Figures S4F–S4J). Other maps show different orientations of those two domains or worse defined densities, specially at the CDC37 MD region. These maps could represent transient conformations waiting for the release and subsequent proper folding of the RAF1 N-lobe (Figure S5A).

In the third approach, both lateral densities of the RHC complex were independently analyzed through masking and local classification and refinement (Relion; Figures S3C and S5B). Ten different classes were obtained when focusing the classification on the RAF1 C-lobe, corresponding those clearly to slightly different rotations of that domain around a fulcrum, constituted by two close elements: the entry point of the extended segment into the HSP90 main body and the interaction of that C-lobe with

the CDC37 ND (Figures 2B and S5B). Another ten classes were obtained when the focus was put on the other lateral blob, but in this case the maps were not as clear as in the case of RHC-II, so not clear details could be extracted about the state of the CDC37 MD and/or RAF1 N-lobe (Figure S5B). Final maps were refined, sharpened and their local resolution estimated in Relion; global resolution was estimated based on the gold-standard Fourier shell correlation 0.143 criterion.

Model building and refinement

Previous models of the HSP90-CDC37-Cdk4 complex (PDB ID: 5FWK), B-Raf:14-3-3 complex (6UAN), CDC37 protein (1US7.) and RAF1 protein (3OMV) were used for the initial interpretation of the maps and preliminary model building. Also, we used Alphafold v2.0 (Tunyasuvunakool et al., 2021) predictions of RAF1 and CDC37. Both the CDC37 CTD and the N-terminal part of RAF1 (~349 aa) were not visible in the cryo-EM maps and probably they are moving freely without additional contacts with the rest of the RHC complex. Initial fitting of the models into the maps was performed with ChimeraX (Goddard et al., 2018). Coot (Emsley et al., 2010) was used for model building, modification, manual local refinement and visualization. An initial model was built in the RHC-I, as this map showed the better density for the HSP90 protomers and the NTD of CDC37. The other moieties of the RHC complex were built using the RHC-II map. The segment of RAF1 in contact with the CDC37 MD was fitted with an extended peptide, while the local resolution in this region did not allow unambiguous model building, several of the bulky side chains helped the assignment of this section of the structure. The HSP90- β isoform was built in our model as it seemed predominant. However, at the current resolution it is difficult to distinguish between the α and β isoforms. Coordinate refinements in real space were performed with Phenix (Adams et al., 2010). Isolde (Croll, 2018) and Namdinator (Kidmose et al., 2019) were used for additional refinements in regions of low-resolution. Figures and videos were generated in ChimeraX and PyMOL <https://pymol.org/2/>.

Western blot analysis and antibodies

For Western blotting, 30 μ g of input and 20 μ l of Strep pull-down eluate coming from Expi293F cells were separated by SDS-PAGE and transferred to nitrocellulose membranes (GE Healthcare). Membranes were probed with antibodies for HSP90 (Santa Cruz sc-13119, 1:1000), RAF1 (BD 610151, 1:1000), CDC37 (Santa Cruz sc-13129, 1:1000), 14-3-3 ϵ (Santa Cruz sc-393177, 1:1000), 14-3-3 ζ (Santa Cruz, sc-293415, 1:1000), A-RAF (Cell Signaling 4432, 1:500), B-RAF (Santa Cruz, sc-5284 1:1000), pan-Ras (Calbiochem OP40, 1:250), and Vinculin (Sigma V9131, 1:5000). Primary antibodies were detected with appropriate secondary antibodies conjugated to HRP and visualized by ECL-Plus (GE Healthcare).

Protein kinase assay

In vitro protein kinase assay was performed after Strep purification of RHC complex expressed in Expi293F cells. 2 μ g of the eluate was used for the kinase reaction, using a commercial RAF1 kinase assay kit (Millipore), following the protocol instructions of the provider. This assay kit is designed to measure RAF1 dependent phosphotransferase activity in a kinase reaction using recombinant inactive MEK1 as a RAF1 substrate. Samples were analysed by SDS-PAGE and the phosphorylation of MEK1 at residues Ser217/221 was detected by Western blotting with a commercial antibody (Cell Signalling #9121, 1:500).

Sample preparation for mass spectrometry and size-exclusion chromatography with multiangle light scattering (SEC-MALS) analysis

For MS-based analysis of RHC complex phosphorylation status, the proteins were resolved by SDS-PAGE, using 4–12% bis-tris gradient gels (Invitrogen), and stained with the Colloidal Blue Kit (Invitrogen) according to manufacturer instructions. For each sample, the RAF1, HSP90 and CDC37 specific bands were excised from the gel in 1 \times 2-mm cubes. Excised SDS-PAGE bands were washed, and proteins digested using the standard in-gel digestion procedure. Briefly, proteins were reduced (25 mM TCEP, 30 min, 45 $^{\circ}$ C) and alkylated (40 mM CAA, 1 h, RT in the dark) and digested with trypsin for 16 hours at 37 $^{\circ}$ C in 50 mM NaHCO₃ (Promega) (estimated protein:enzyme ratio 1:100). Digestion was quenched with 0.1% TFA and resulting peptides were desalted using C₁₈ stage-tips. In the case of proteins in solution, samples were digested by means of standard FASP protocol. Briefly, proteins were alkylated (50 mM CAA, 20 min in the dark, RT) and sequentially digested with Lys-C (Wako) (estimated protein:enzyme ratio 1:100, o/n at RT) and trypsin (Promega) (estimated protein:enzyme ratio 1:100, 6 hours at 37 $^{\circ}$ C). Resulting peptides were desalted using C₁₈ stage-tips.

LC-MS/MS was carried out by coupling an UltiMate 3000 RSLCnano LC system to either a Q Exactive Plus or Q Exactive HF mass spectrometer (Thermo Fisher Scientific). In both cases, peptides were loaded into a trap column (Acclaim™ PepMap™ 100 C18 LC Columns 5 μ m, 20 mm length) for 3 min at a flow rate of 10 μ l/min in 0.1% FA. Then, peptides were transferred to an EASY-Spray PepMap RSLC C18 column (Thermo) (2 μ m, 75 μ m \times 50 cm) operated at 45 $^{\circ}$ C and separated using a 60 min effective gradient (buffer A: 0.1% FA; buffer B: 100% ACN, 0.1% FA) at a flow rate of 250 nL/min. The gradient used was, from 2% to 6% of buffer B in 2 min, from 6% to 33% B in 58 minutes, from 33% to 45% in 2 minutes, plus 10 additional minutes at 98% B. Peptides were sprayed at 1.5 kV into the mass spectrometer via the EASY-Spray source and the capillary temperature was set to 300 $^{\circ}$ C.

The Q Exactive Plus mass spectrometer was operated in a data-dependent mode, with an automatic switch between MS and MS/MS scans using a top 15 method. (Intensity threshold \geq 4.5e4, dynamic exclusion of 10 sec and excluding charges unassigned, +1 and > +6). MS spectra were acquired from 350 to 1500 m/z with a resolution of 70,000 FWHM (200 m/z). Ion peptides were isolated

using a 2.0 Th window and fragmented using higher-energy collisional dissociation (HCD) with a normalized collision energy of 27. MS/MS spectra resolution was set to 35,000 (200 m/z). The ion target values were 3e6 for MS (maximum IT of 25 ms) and 1e5 for MS/MS (maximum IT of 110 msec).

The Q Exactive HF mass spectrometer was operated as described above for the Q Exactive Plus mass spectrometer except using an Intensity threshold $\geq 2.2 \times 10^4$, dynamic exclusion of 10 sec and excluding charges +1 and $> +6$. MS spectra were acquired from 350 to 1400 m/z with a resolution of 60,000 FWHM (200 m/z). Ion peptides were isolated using a 2.0 Th window and fragmented using higher-energy collisional dissociation (HCD) with a normalized collision energy of 27. MS/MS spectra resolution was set to 30,000 (200 m/z). The ion target values were 3e6 for MS (maximum IT of 25 ms) and 1e5 for MS/MS (maximum IT of 45 msec).

Size-exclusion chromatography with multiangle light scattering (SEC-MALS) analysis

The oligomeric state and stoichiometry of the RHC complex were analysed by SEC-MALS analysis. Protein samples were prepared as described previously. 105 μg of sample (at 0.7 mg/mL) were injected in a Superdex 200 10/300 size exclusion column (GE Healthcare) equilibrated in buffer A1. Data were collected on Dawn Heleos 8+ and Optilab Trex detectors and analyzed using ASTRA6 software (Wyatt Technology). The monomeric BSA (Sigma-Aldrich) was used as standard to verify instrument performance.

CDC37 purification and binding assays on cellulose-bound peptides containing RAF family sequences

The human full-length CDC37 cDNA was amplified by PCR with restriction site-tailed primers incorporating a C-terminal StrepTagII, separated from protein by a Gly-Ser-Ala residue linker from the Origene RC201002 plasmid. The resulting DNA was cloned into the HindIII/XhoI sites of the transfer vector pcDNA3 (Invitrogen), using the In-Fusion® HD EcoDry Cloning Kit (Takara Bio USA). The derivative plasmid, pcDNA3-CDC37-Strep, was sequence verified. Four 120 ml cultures of Expi293F cells were transfected with 120 μg of pcDNA3-CDC37-Strep plasmid using the ExpiFectamine 293 Transfection Kit as described for the RHC complex. After the first step of protein purification by affinity chromatography, CDC37-containing fractions were pooled, concentrated to < 5 ml with a 10-kDa Vivaspin concentrator (Sartorius), and further purified by size exclusion chromatography (SEC) with a Superdex S75 16/600 column (GE Healthcare) in buffer A1, using an ÄKTA FPLC system (GE Healthcare). The eluted peak corresponding to CDC37 protein was collected and concentrated with a 10-kDa Vivaspin concentrator to final concentration of about 2 mg/ml and stored at -80°C until use.

Overlapping dodecapeptides scanning the kinase domain sequence of human A-RAF, B-RAF and RAF1 were prepared by SPOT-Synthesis (JPT, Berlin, Germany) onto a cellulose- β -alanine-membrane (Table S3). The membranes were rinsed with methanol, washed with TBS-T and blocked for 2 hours using 2.5% BSA. The saturated membranes were incubated with purified CDC37 protein (10 $\mu\text{g}/\text{ml}$) for 3 hours and after several washing steps with TBS-T, incubated with anti-CDC37 antibody (Santa Cruz Biotechnology), followed by HRP-conjugated secondary antibody (Dako). Positive spots were visualized using the ECL system (Bio-Rad). Dots from the scanned films were quantified using the software ImageJ. To compare among the three RAF family members, a peptide with a common sequence was selected for normalization (peptide 18 from region #3). CDC37 binding affinity to each peptide was calculated as the mean pixel integrated density of each dot relative to a reference one.

Site-directed mutagenesis and pull-downs from cell lysates

All RAF1 and CDC37 constructs expressed in mammalian cells for Figures 3 and 6 were generated by QuickChange Lightning Site-Directed Mutagenesis (Agilent Technologies), using the primer sequences shown in Table S4. RAF1 mutants including L459E, I464E, K483A, I484A, D486A, F487A, F487R and F487E were generated from pcDNA3-RAF1-Strep plasmid. Human RAF1-CAAX cDNAs carrying the D486A, F487A and D486A/F487A mutations used for retroviral expression in K-Raslox MEFs were generated from pBABE-puro-Raf1-WT-CAAX plasmid. The CDC37 I23E mutant was generated from pcDNA3-CDC37-Strep plasmid.

For the generation of RHC complexes carrying the above RAF1 mutants, 20 ml cultures of Expi293F cells were transiently transfected with 20 μg plasmid DNA (10 μg pcDNA3-RAF1-Strep wt or mutant variant + 5 μg pcDNA3-HSP90-HA + 5 μg of pCMV6-CDC37-Myc-DDK) using polyethylenimine (PEI) (Polysciences Inc.). Cells were harvested 48 h after transfection. Pellets were lysed as described before. 20 mg of total protein extracts were incubated with 200 μl pre-washed Strep-Tactin resin (IBA GmbH) for 1 hour at 4°C . Resin was spun down (1000 \times g for 30 s) and washed five times with 500 μl buffer A1. Proteins were eluted from the Strep-Tactin matrix with 2 \times 100 μl of buffer A1 supplemented with 5 mM desthiobiotin for 10 min on ice. For the CDC37 interaction mutant experiment, 20 ml cultures of Expi293F cells were transiently transfected with 20 μg plasmid DNA (10 μg pcDNA3-RAF1-His + 5 μg pcDNA3-HSP90-HA + 5 μg of pcDNA3-CDC37-Strep wt or I23E) using PEI and processed as described for RAF1 mutants. In both cases, eluates were analysed on SDS-PAGE, followed by Western blotting with specific antibodies and staining with Coomassie blue. To get an accurate quantification of the proteins, part of the eluate was analysed by Mass Spectrometry.

Processing and analysis of mass spectrometry data

Raw files were processed with MaxQuant using the standard settings against a human protein database (Swiss-Prot, 20,373 sequences) containing the recombinant protein sequences used in this work and supplemented with contaminants. Carbamidomethylation of cysteines was set as a fixed modification whereas oxidation of methionines, protein N-term acetylation and phosphorylation of serines, threonines and tyrosines were set as variable modifications. Minimal peptide length was set to 7 amino acids and a maximum of two tryptic missed cleavages were allowed. Results were filtered at 1% FDR (peptide and protein level).

For RAF1 pull down experiments, the normalization factor was calculated by adding the intensities of all the RAF1 peptides whose sequences are shared by all RAF1 mutants, excluding those sequences in which a phosphorylation site was identified. For the CDC37 pull down, the normalization factor was calculated by summing the intensities of all the CDC37 peptides whose sequences are shared by all CDC37 mutants.

Colony assay in *Rasless* and *Rafless* MEFs

Low passage (p12-15), immortal *H-Ras*^{-/-}; *N-Ras*^{-/-}; *K-Ras*^{lox/lox} (K-Raslox) and *A-Raf*^{lox/lox}; *B-Raf*^{lox/lox}; *Raf1*^{lox/lox} (Raflox) MEFs were infected with retroviral and lentiviral supernatants, respectively, and selected with the appropriate antibiotic as described earlier (Martín et al., 2005). Resistant cells were seeded in equal cell number (3,000-6,000) in the absence or presence of 4-hydroxytamoxifen (4OHT, Sigma, 600 nM). Cells were allowed to form colonies for 14 days. Plates were fixed with 1% glutaraldehyde (Sigma), stained with crystal violet (Merk), and colonies > 2 mm in diameter scored. When needed, representative colonies were picked and expanded for further analysis. In addition to the indicated cDNAs, all K-Raslox cells were infected with a retrovirus encoding a shRNA directed against p16INK4a-specific sequences, to prevent cellular senescence (Drosten et al., 2010). This step was skipped in Raflox cells.

QUANTIFICATION AND STATISTICAL ANALYSIS

Quantification of signal from PepScan assay was performed using the integrated density function of ImageJ 1.52a (Schneider et al., 2012). The exact quantifications are described in the STAR Methods section. All graphs and diagrams derived from quantification were generated in Excel. All quantitative data are presented as the mean values while the error bars represent the standard deviation of three independent experiments, unless stated otherwise. No statistical analysis was carried out in this study.